Rune Natten Kleiveland

Modelling of Soot Formation and Oxidation in Turbulent Diffusion Flames

Doctoral thesis
for the degree of doktor ingeniør

Trondheim, September 2005

Norwegian University of
Science and Technology
Faculty of Engineering Science and Technology
Department of Energy and Process Engineering

NTNU
Innovation and Creativity

NTNU
Norwegian University of
Science and Technology

Doctoral thesis
for the degree of doktor ingeniør

Faculty of Engineering Science and Technology
Department of Energy and Process Engineering

ISBN 82-471-7240-2 (printed ver.)
ISBN 82-471-7239-9 (electronic ver.)

Doctoral Theses at NTNU,

Printed by Tapir Uttrykk

Abstract

Soot and radiation play an important role when designing practical combustion devices, and great efforts have been put into developing models which describe soot formation and oxidation. The Eddy Dissipation Concept (EDC) has proven to describe turbulent combustion well, and has the flexibility to describe chemical kinetics in a detailed manner. The aim of this work is to study how the EDC handles soot models based on a detailed representation of the gas-phase chemical kinetics.

Two versions of a semi-empirical soot model is used in conjunction with the EDC. Concentrations of various intermediate species are used as input to the soot models.

The implementation of the new soot models is discussed in relation to the previous implementation of a less detailed soot model. To assure that the interaction between soot and the gas-phase species is represented correctly, the soot models are implemented with a two-way coupling of soot and gas-phase kinetics.

Soot is a good radiator. In a sooting flame a substantial amount of energy will be transferred to the surroundings by thermal radiation. This transfer of energy will alter the temperature field of the flame and the change in temperature will affect the kinetics of soot and gas-phase chemistry. To simulate sooting flames correctly, it was therefore necessary to include a radiation model.

To validate the coupled models of turbulence, combustion, soot, and radiation two different turbulent flames were simulated. One turbulent jet flame of methane and

one turbulent jet flame of ethylene. For both flames the computed results were compared with measured values.

Several aspects of the simulations are studied and discussed, such as the effect of the two-way coupling of soot and gas-phase kinetics on both soot yield and gas-phase composition, and the importance of a suitable radiation model.

The two-way coupling of soot and gas phase kinetics is shown to have a positive effect on the computed soot volume fractions, and the results are considered to be encouraging. The work has demonstrated that the EDC has the capacity to handle different types of chemical reaction mechanisms, such as mechanisms for gas-phase combustion and soot kinetics, without modification.

Preface

This thesis is the result of my Doctor of Engineering study at the Department of Energy and Process Engineering. My study has been made possible by financial support from Vista[1] and SINTEF Energy Research AS.

I would like to thank to my supervisors Professor Bjørn F. Magnussen and Professor Inge R. Gran for their continuous enthusiasm and interest in my work. By sharing their tremendous knowledge and deep understanding of the subject area with me, this study has been a wonderful and fascinating experience in science.

I am also grateful to Associate Professor Ivar S. Ertesvåg for many helpful discussions and for reading parts of the manuscript. Dr. Jochen Ströhle has also read parts of the manuscript and has enlightened me in the complex field of gaseous radiation.

I am pleased to express my acknowledgment to Professor J. B. Moss and Dr. S. J. Brookes at Cranfield University for providing their experimental data on electronic format.

[1] Vista is a research collaboration between The Norwegian Academy of Science and Letters and Statoil

Finally, I would like to give special thanks to my beloved family, Kine, Signe, and Elise.

This thesis will be submitted for the degree:

Doktor Ingeniør (Dr. ing.)
Doctor of Engineering

at the Norwegian University of Science and Technology (NTNU).

Trondheim, September 2005

Rune Natten Kleiveland

Contents

Nomenclature

Latin letters

A_i	representation of the chemical species i
A_l	preexponential factor in the Arrhenius rate expression for reaction l
a	model constant in the Tesner/EDC soot model
a_0	constant in the Tesner/EDC soot model
a_P	Planck mean absorption coefficient
a_P, a_{nb}, a_f	coefficients in the discretizised equation
a_λ	absorption coefficient
$a_{\lambda,\mathrm{S}}$	absorption coefficient of soot particles
b	model constant in the Tesner/EDC soot model
b	source term in the discretisised equation
b_j	potential energy in the x_j-direction
b_l	temperature exponent in the Arrhenius expression for reaction l
C_1, C_2	constants in the Planck distribution
C_a	agglomeration rate constant
C_{D1}, C_{D2}	model constants in the EDC model
C_{min}	number of carbon atoms in the incipient soot particle
$C_{\varepsilon 1}$, $C_{\varepsilon 2}$, C_μ	constants in the k-ε turbulence model
$C_{\varepsilon 3}$	constant in the round-jet version of the k-ε turbulence model
c_λ	constant in the expression for the absorption coefficient of soot particles

c_0	speed of light in vacuum
c_k	concentration of species k in the mixture
$c_{p,k}$	specific heat capasity at constant pressure for spcies k
D	Diffusion coefficient of the mixture
d_p	diameter of a soot particle
$E_{a,l}$	activation energy in the Arrhenius expression for reaction l
$e\lambda, b$	spectral emissive power from a perfect radiator
e_t	specific total energy
F_j	force acting on the system in the x_j-direction
f	linear branching coefficient
f_c	mass fraction of carbon in the fuel
g	linera termination coefficient
g_0	coefficient of linear termination on soot particles
h	specific enthalpy
h	universal Planck constant
h_k	specific enthalpy of species k
h_k°	specific enthalpy of formation of species k
j_j^k	diffusion flux of species k in the x_j-direction
j_j^q	total energy flux in the x_j-direction
$(j_c^q)_j$	energy flux in the x_j-direction due to conduction
$(j_D^q)_j$	energy flux in the x_j-direction due to concentration gradients
$(j_d^q)_j$	energy flux in the x_j-direction due to species diffusion
K	coagulation rate constant
k	universal Boltzmann constant
$\tilde{k}$	turbulence kinetic energy
k_l	velocity coefficient of reaction l
L^*	characteristic length for the fine structures in the EDC model
L'	characterisic length for the large scale turbulent eddies
Le	Lewis number
M	molecular mass
M_k	molecular mass of species k

M_s	molar mass of soot
m_p	mass of a soot particle
$\dot{m}^*$	mass exchange rate of between the fine structures and surroundings
N_A	Avogadro's number
n	concentration of radical nuclei
n_{cr}	number of chemical reactions
n_0	spontaneous origination rate of radical nuclei
n_s	number of species
P_k	production rate of turbulence kinetic energy
p	pressure
Q	production rate of thermal energy
Q_{emi}	Emitted energy by radiation from a volume
Re	Reynolds nummber
R_i	representation of a process in the Lindstedt/Moss soot model
R_u	universal gas constant
r	radius
r_{F}	stoichiometric amount of oxidiser in the one-step infinitely fast combustion reaction
S	concentration of soot
S	soot surface area
S_i	source term in the general transport equation
S_ε	source term in the round-jet version of the ε-equation
S_{1P}	constant part of the source term in the discretisised equation
S_{2P}	variable part of the source term in the discretisised equation
T	temperature
T_b	temperature of surroundings
u	specific internal energy
u^*	characteristic velocity for the fine structures in the EDC model
u'	characteristic velocity for the large scale turbulent eddies
v_i	Cartesian velocity component in the x_i-direction
X_k	mole fraction of species k

x_j	Cartesian coordinate
Y_i	mass fraction of species i
Y_{N}	particle number density of soot particles
Y_n	mass fraction of radical nuclei
Y_s	mass fraction of soot
$Y_{s,\max}$	model parameter in version II of the tesner/EDC soot model
$\tilde{Y}_{\mathrm{F}}$, $\tilde{Y}_{\mathrm{O}}$, $\tilde{Y}_{\mathrm{P}}$	mass fractions of fuel, oxidiser, and product
$\tilde{Y}_{\min}$	The maximum amount of fuel that can be converted into products in the one-step infinitely fast combustion reaction
y	correction coefficient in expression for the coagulation rate constant

Greek letters

β	temperature exponent in the modified Arrhenius expression
Γ_{eff}	Effective diffusion coefficient
Γ_i	Diffusion coefficient in the general transport equation
γ_λ	fraction of the flow occupied by fine structure regions
γ^*	fraction of the flow occupied by fine structures
δ_{kj}	Kronecker delta
$\tilde{\varepsilon}$	rate of disspiation of turbulence energy
κ	Boltzmann constant
λ	thermal conductivity
λ	wavelength
μ	viscosity of the mixture
μ_B	bulk viscosity
μ_{eff}	effective viscosty
μ_k	viscosity of species k
μ_t	eddy viscosity
ν	kinematic viscosity
ν_t	kinematic eddy viscosity
ν'_{il}	stoichiometric coefficient of reactant species i in reaction l

ν''_{il}	stoichiometric coefficient of product species i in reaction l
r_{F}	stoichiometric amount of oxidiser
ρ	density
ρ_s	density of soot
σ	Stefan-Boltzmann constant
σ	Prandtl number
σ_k	constant in the k-ε turbulence model
σ_t	turbulence Prandtl-Schmidt number
σ_y	Schmidt number
σ_ε	constant in the k-ε turbulence model
τ_{kj}	viscous stress tensor
Φ	stationary potential
ϕ_i	general scalar variable
φ	general variable
χ	fraction of fine structures where reaction occurs
χ_1, χ_2, χ_3	factors in the model expression for χ
ω	net chemical production rate of a gas-phase species or soot
$\dot{\omega}^*_{i,s}$	consumption rate of species i due to soot kinetics
ω_k	chemical production rate of species k

Subscripts

b	bottom cell face
c	combustion
e	east cell face
f	formation
fu	fuel
F	fuel
n	radical nuclei

n	north cell face
NO	non-orthogonal
O	oxidant
P	product
P	main node point
s	soot
t	top cell face
w	west cell face

Superscripts

$'$	reactant
$'$	fluctuating value, Reynolds averaging
$''$	product
$''$	fluctuating value, density-weighted averaging
-	mean
$\sim$	density-weighted mean
$*$	EDC fine structure state
$\circ$	surroundig state
$\circ$	previous time step
I	version I of the Tesner/EDC soot model
II	version II of the Tesner/EDC soot model

Abbreviations

CPU	central processing unit
EDC	eddy dissipation concept
HACA	H-abstraction, C_2H_2-addition, reaction sequence for soot growth
PAH	polycyclic aromatic hydrocarbons
pdf	probability density function
POW	power-law scheme
SOU	second-order upwind scheme

Chapter 1

Introduction

1.1 Motivation for the Thesis

Understanding the processes controlling soot in combustion has been an important research field for more than three decades. There are several reasons for this interest. In most combustion processes soot is an undesirable product. Soot particles in the exhaust gas of a combustion engine are a result of incomplete combustion, indicating poor utilisation of the fuel. Soot which is released into the atmosphere also represents a threat to the environment and the health of human beings. Soot is believed to be formed from large polycyclic aromatic hydrocarbons (PAH) and many of these molecules are known to have a carcinogenic effect [2]. In industrial reactors where combustion or partial combustion is taking place, deposition of soot may lead to stacked process equipment. An example of a process where this can be a problem is the production of methanol from natural gas. In this process a synthesis gas with a high concentration of methane is oxidised in a reforming reactor with an under-stoichiometric amount of air [86]. If the parameters controlling the combustion and soot formation such as mixing, temperature, and composition of fuel and oxidiser, are not correctly tuned, soot will start to deposit on the reactor catalyst. The equipment will need to be cleaned or replaced and

production has to be halted, resulting in an economic loss.

However, soot is not only an unwanted byproduct of combustion. In some combustion processes a controlled amount of soot is desired. Soot in a flame greatly enhance the energy transfer from the flame to its surroundings by radiation. This is often a desired feature in furnaces where the objective is to transfer the heat from the flame to the furnace walls. In such cases it is, however, important to control the combustion in such a way that the soot particles are oxidised before the exhaust gas is released into the atmosphere.

Soot formation and oxidation are highly complex processes, involving a large number of both homogeneous and heterogeneous chemical reactions and other physical processes such as coagulation and agglomeration. The most sophisticated soot models of today describe all these processes in an detailed manner. These models can predict soot in laminar flames with a high degree of accuracy [1, 26]. However, these models are expensive in terms of CPU time, even for simulations of laminar flames. In predictions of turbulent combustion, the detailed soot models have to be used together with other models necessary to describe reacting turbulent flow, leading to a very high CPU-cost even for simple flames. Thus, for predictions of soot in practical engineering equipment it is often necessary to use simplified models to keep CPU-cost at an acceptable level.

1.2 Previous work

An extensive amount of both experimental and theoretical work on soot in flames is reported in the literature. A comprehensive review of major results and findings up to 1981 is given by B. S. Haynes and H. Gg. Wagner [40]. More recent reviews on the subject have been given by I. Glassman [33] (1988) and M. Frenklach [26] (2002). The major focus of Glassman is experimental results while Frenklach emphasises on the chemical reaction mechanism of soot formation. Several different approaches for modelling soot formation and oxidation has been published, and a thorough review is given by I. M. Kennedy in an article from 1997 [50]. Another comprehensive source of theory and experimental results on soot is the book *Soot*

Formation in Combustion [5]. This book is a collection of papers presented at the workshop "Mechanism and Models of Soot Formation" held in Heidelberg, Germany, in October 1991.

Some of the earliest work on soot formation in turbulent combustion was predictions of soot in exhaust gas from engines such as diesel engines [48] and gas turbines [19]. These were empirical models with limited description of the actual physical and chemical processes taking place. The use of these models was also restricted to certain types of engines and specific fuels. Today it has become common to use more detailed models even for simulations of turbulent combustion. Due to the need for simple and well defined test cases, these detailed, or semi-empirical, soot models are usually developed and tested for laminar flames. The soot models are then incorporated in existing codes for turbulent combustion. One of the first to apply this strategy was Magnussen and Hjertager who used a soot model by Tesner together with his "Eddy Dissipation Concept" combustion model [65].

During the last decade there has been focus on rather simple semi-empirical soot models used in conjunction with pdf- and flamelet-based combustion models, examples are Young et al. [102], Fairweather et al. [22, 23], Kollmann et al. [52], Brookes et al. [13], and Kronenburg et al. [53]. A more detailed presentation of the works of Brookes et al. [13] and Kronenburg et al. [53] is given in Chapter 6. The soot models used in these works are rather similar, however, the soot models are used with different combustion models. This linking of soot kinetics to turbulence and gas-phase chemistry is crucial for the success of the simulations. At present, the task of modelling the interaction of turbulence, gas-phase chemistry and soot kinetics is probably the major challenge in predictions of soot in turbulent combustion.

Recently, there has been published results from simulations of turbulent combustion where more detailed and complex soot models have been used. Balthasar et al. [1] used a detailed soot model to simulate soot formation in a turbulent partially stirred plug flow reactor. The gas-phase reaction scheme and soot model was based on works of Frenklach and Wang [29] and Mauss et al. [67], and the turbulent combustion was modelled by solving an equation for the joint

scalar probability density function (PDF). Pitsch et al. [79] used basically the same soot model, but with an unsteady flamelet combustion model, to predict soot in an turbulent diffusion flame of ethylene. A more detailed presentation of the work of Pitsch et al. [79] is given in Chapter 7.

To appraise a models ability to predict soot in turbulent combustion, it is of course, necessary with reliable experimental data. However, the amount of experimental data from turbulent flames, reported in the literature is limited. Today most measurements of soot variables in flames are done with different laser-based techniques such as laser extinction tomography. Examples of recent measurements of soot in turbulent flames are; Kent et al. [51] and Coppalle et al. [16, 17] who have studied turbulent diffusion flames of ethylene while Brookes et al. [11] have worked with turbulent diffusion flames of methane. The works of Brookes et al. [11] and Kent et al. [51] is used to validate the present modelling approach, presented in Chapters 6 and 7 respectively.

1.3 Present Contribution

The main contributions of this thesis are:

- Two versions of a semi-empirical soot model are included in the EDC combustion model. The soot models are used together with a detailed representation of the gas phase chemistry.
- The implementation of the soot models includes a two-way coupling of soot and gas-phase chemistry.
- The implementation of the soot models is independent of the type of soot models. This makes it possible to exchange the soot models used in the present work with other models. The work can be regarded as a framework for testing soot models in turbulent combustion.
- A simple radiation model is included in the EDC combustion model.

- Predictions of soot volume fractions in two turbulent diffusion flames with different fuels are presented.
- The effect of the two-way coupling of the soot model on soot formation and on gas-phase composition is studied.
- The effect of radiation on soot formation and temperature is studied.

1.4 Survey of the Thesis

In the first part of Chapter 2, a short review of the basic steps of soot formation and oxidation in combustion is given. The basic physics of the different processes taking place are also presented. In the last part of Chapter 2 two different semi-empirical soot models are presented. Two versions of the latter of these models are used in the present calculations.

In Chapter 3 the physical fundamentals which are the basis of the simulations, are presented. This includes modelling of molecular transport, conservation equations, and treatment of chemical reactions and radiation.

Chapter 4 deals with modelling of turbulent combustion. The conservation equations are averaged and the closure of the Reynolds stresses using the k-ε model, is presented. The modelling of the chemical source term in the averaged equations for species conservation is presented. This averaged source term is calculated by use of the "Eddy Dissipation Concept" (EDC). A detailed presentation of the background and use of the EDC with a detailed representation of chemical kinetics is given. Strategies for inclusion of soot models into the EDC is discussed and a method for a two-way coupling of soot and gas-phase chemistry is presented. Methods for incorporation of radiation models into the EDC is shown and discussed.

Chapter 5 presents the numerical methods employed to implement the various mathematical models.

In Chapter 6 a turbulent diffusion flame of methane is studied. Predictions of tem-

perature, mixture fraction and soot volume fractions are compared to experimental results. The effect of a two-way coupling of soot and gas-phase chemistry on both soot yield and gas-phase composition is investigated. Also, the effect of radiation on predicted temperatures and soot volume fractions is studied.

Chapter 7 presents results from simulations of a turbulent diffusion flame of ethylene. Predicted values of temperatures and soot volume fractions are compared with measurements. As for the methane flame, effects of two-way coupling of soot and gas-phase chemistry and radiation are studied.

In Chapter 8 conclusions and suggestions for further work are given.

Chapter 2

Soot in combustion

2.1 Physical Picture of Soot Formation

Examining some of the experimental results on soot formation in combustion, it is soon apparent that soot from different flames may be very different. The size and structure of soot varies from almost spherical particles containing only a few atoms to large aggregate structures containing some millions of atoms. Common for the various appearances of soot is that it mostly consist of carbon and small amounts of hydrogen, up to 10 wt% of hydrogen. Despite the lack of a unique chemical or physical structure, a majority of the scientists involved in soot research agrees that the basic physical and chemical processes taking place in soot formation, are the same regardless of fuel or type of flame [33]. Even though there is consensus about the major steps of soot formation, the details of the underlying physics of some of these processes are still not clear. Soot formation in flames can be divided into five different steps. A short description of these steps is given below.

2.1.1 Particle Inception

At some point in a sooting flame, solid soot particles are formed from gas-phase species. This transition from gas-phase species to solid soot particles is probably the least understood part of the soot formation process. Several mechanisms for the formation of the first soot particles have been proposed, using charged species [15, 25], polyacetylenes [6, 24, 44] and polycyclic aromatic hydrocarbons as precursors to soot particles. At present the majority of soot models is based on the assumption that the soot particles are formed from large polycyclic aromatic hydrocarbons (PAH) [26, 33, 40]. Michael Frenklach and his co-workers have for several years studied and modelled soot formation via PAH and the presentation on soot inception given below is mostly based on their work. The soot particle inception process is believed to be controlled by the formation and growth of these ring-formed molecules. In this growth process the formation of the first ring is believed to to be rate-limiting [27] and the kinetics describing the formation of this ring has been the subject of several studies. There are still uncertainties connected to which routes to the first aromatic ring that are most important under different conditions. The following reactions have in several studies been found to be important [27, 30, 71, 26, 61]. The relative importance of these reactions are still not fully determined.

$$\text{n-}C_4H_3 + C_2H_2 \longrightarrow \text{phenyl} \tag{2.1}$$

$$\text{n-}C_4H_5 + C_2H_2 \longrightarrow \text{benzene} + H \tag{2.2}$$

$$C_3H_3 + C_3H_3 \longrightarrow \text{benzene} \tag{2.3}$$

$$C_3H_3 + C_2H_2 \longrightarrow \cdots \longrightarrow \text{benzene} \tag{2.4}$$

In all these reactions, except reaction 2.3 acetylene (C_2H_2) is a reactant. Accordingly, acetylene is supposed to be a key species in formation of the first aromatic ring.

The further growth of PAH is complex and requires a large reaction scheme for a detailed description [30]. To make it possible to predict soot in practical flames, simplifications has to be made. Based on data from shock-tube experiments Frenklach and Wang [28] presented a simplified mechanism for growth of PAH in

flames. The mechanism consist of a repetitive reaction sequence of two steps. Abstraction of a hydrogen atom from the reacting hydrocarbon followed by addition of an acetylene molecule to the radical site formed. The reaction sequence is named HACA which is an acronym for H-abstraction-C_2H_2-addition. The basic reaction sequence can be represented as [29, 26]

$$A_i + H \rightleftharpoons A_{i-} + H_2 \tag{2.5}$$

$$A_{i-} + C_2H_2 \rightleftharpoons A_iC_2H_2 \tag{2.6}$$

$$A_iC_2H_2 + C_2H_2 \rightarrow A_{i+1} + H \tag{2.7}$$

where A_i represents an aromatic molecule containing i rings and A_{i-} and $A_iC_2H_2$ are aromatic radicals. In the complete HACA sequence the radical A_{i-} may also react with other species than acetylene, forming products not leading to PAH growth.

As evident from reactions 2.5 – 2.7 the species responsible for PAH growth in the HACA sequence is acetylene. Aromatic rings may also grow by reactions with other species than acetylene [26] but both experimental and modelling results indicate acetylene as the most important growth species.

When the aromatic compounds reach a certain size they can also grow by sticking to each other growing into larger clusters and eventually evolve into solid particles.

2.1.2 Mass Growth and Oxidation

Nucleation of soot particles is of course a key factor in determining the amount of soot particles. However, most of the soot mass is not a result of nucleation, but of reactions between the soot particles and gas-phase species [40]. Gas-phase species are believed to react on active sites on the surface of the soot particles. Several gas-phase species has been suggested as important growth species, but experimental results indicate acetylene as the most important growth species [39, 101].

Gas-phase species do not only contribute to soot growth. The soot particles will also be oxidised by gas-phase species. Experimental studies have pointed out O_2 and OH as the most important oxidisers of soot in flames [76, 82, 100, 32]

The details of soot mass growth and oxidation are still unclear, but Frenklach and Wang used the HACA sequence to model the soot mass growth by acetylene. This heterogenous version of HACA can be expressed as [28, 29]

$$C^i_{soot-H} + H \rightleftharpoons C^i_{soot-} + H_2 \tag{2.8}$$
$$C^i_{soot-} + H \rightarrow C^i_{soot-H} \tag{2.9}$$
$$C^i_{soot-} + C_2H_2 \rightarrow C^{i+2}_{soot-H} + H \tag{2.10}$$
$$C^i_{soot-} + O_2 \rightarrow \text{products} \tag{2.11}$$
$$C^i_{soot-} + OH \rightarrow \text{products} \tag{2.12}$$

where C^i_{soot-H} represents an active site on the soot surface particle and C^i_{soot-} is the corresponding radical. The HACA scheme has been used to model growth of PAH and soot in several laminar flames with promising results. The HACA sequence also provides a simplified picture of what is believed to be the basic kinetics in soot formation at present.

2.1.3 Coagulation and Agglomeration

Once formed, the soot particles will collide and stick to each other forming larger particles. Experimental results have shown that when relatively small particles collide, they will coalesce into a larger nearly spherical particle. This particle growth mechanism is called coagulation. The rate of coagulation is determined by the frequency of collisions. This frequency can be described by the Smoluchowski equation [91]. Assuming mono-disperse spherical particles, the coagulation rate can be written [98]

$$\left(\frac{\partial n}{\partial t}\right)_{coag} = \frac{1}{2} K n^2 \tag{2.13}$$

where n is the number density of soot particles. K is the coagulation rate constant. The expression for K is dependent on the Knudsen number, that is the ratio of the mean free path to the particle radius. If the Knudsen number is large (particle radius is much smaller than the mean free path), the coagulation is said to be in the free-molecular regime and the collision frequency is governed by kinetic

theory. If the Knudsen number is low, coagulation is in the continuum regime and the collision frequency is determined by particle diffusion. The mechanisms of both these regimes are well understood. However, if the radius of the soot particles is of the same size as the mean free path, coagulation is said to be in the transition regime and models for this regime are complex [31]. Coagulation of soot particles are often assumed to be in the free-molecular regime [40, 9], but this assumption has been questioned [26], especially for combustion at high pressure. If coagulation is in the free-molecular regime, the coagulation rate constant takes the form

$$K = 16r^2 y \left(\frac{\pi \kappa T}{m}\right)^{\frac{1}{2}} \tag{2.14}$$

where r is the radius of the particles, κ is the Boltzmann constant, m is the particle mass, and y is a correction coefficient for interparticle forces.

When larger particles collide, experimental results indicate that they will not coalesce, but rather form chains and grow into larger soot aggregates. The mechanisms governing transition from coagulation growth to aggregation growth are not clear but have been related to the rate of soot surface growth and the size of the soot particles [40, 98]. When the colliding particles are small, surface growth will quickly smoothen the surface of the new particle, giving it a spherical shape. For larger particles, surface growth is not sufficiently fast to smoothen the shape of the particles and they grow into agglomerates. It has also been observed that surface growth is slower on old and large soot particles than on smaller particles. Another physical explanation for the coagulation and agglomeration growth is that the small early soot particles are viscous droplets. When colliding, they will easily coalesce into a new spherical droplet. As the particle size increase the droplets will pyrolyse into solid particles and further collisions will lead to agglomeration growth.

2.2 Semi-Empirical Soot Models

As described in the previous section, the physical and chemical mechanisms leading to soot in flames are numerous and complex. If the intention is to simulate a sooting flame, these mechanisms have to be modelled into a soot model. The soot model must then be used in conjunction with models for all other phenomena which influence the flame, such as convection, diffusion, turbulence, chemical reactions, radiation, and others. All these sub-models make a numerical code for simulating flames complex and often lead to long computation times. This is in particular a challenge when simulating turbulent flows in practical combustion devices. In such cases it is often necessary to use a simplified soot model which is based on experimental data, but at the same time has a physical basis. Such models are called semi-empirical models.

2.2.1 Tesner and Magnussen

In 1971 Tesner and co-workers [94] presented a soot model based on measurements of soot particle formation in diffusion flames of an acetylene-hydrogen mixture. The soot model was also applied to diffusion flames of other hydrogen-hydrocarbon mixtures [95]. Magnussen made some modifications to Tesner's soot model and included it into his EDC model for turbulent combustion. Magnussen also developed a model for soot oxidation which was used together with Tesner's formation model [62, 65]. This modification of the soot model by Tesner will be refered to as the original EDC soot model. No results from simulations with the original EDC soot model are presented in the present work. A description of this model is still presented, both as a reference and as a basis for including other soot models into the EDC.

Two versions of the original EDC soot model are presented below. The model referred to as version I is the original model by Magnussen. Version II is the latest version developed by Magnussen and Lilleheie [59]. The subscripts $_{\mathrm{I}}$ and $_{\mathrm{II}}$ in the model expressions refer to the different versions of the model.

Version I

The soot model by Tesner is a two-step model where soot (s) is formed from radical nuclei (n). To simplify the presentation of the model the total rate expressions of nuclei and soot are split into formation (f) and combustion (c).

$$\omega_{\mathrm{n/s}} = \omega_{\mathrm{n/s,f}} + \omega_{\mathrm{n/s,c}} \tag{2.15}$$

The formation and consumption of radical nuclei are modelled as a chain type radical processes. Tesner's equation for formation of radical nuclei bears a strong resemblance with Semenov's equation for a branched-chain reaction with quadratic terminations, and can be written as [94]

$$\omega_{\mathrm{n,f,I}} = \frac{1}{\rho}\frac{dn}{dt} = \frac{n_0}{\rho} + (f-g)Y_{\mathrm{n}} - \rho\frac{g_0}{m_p}Y_{\mathrm{n}}Y_{\mathrm{s}} \quad \left[\frac{\text{particles}}{\text{kg}\cdot\text{s}}\right] \tag{2.16}$$

where

n - concentration of active particles involved in the process (part./(m^{3}s))
n_0 - spontaneous origination rate of active particles (part./(m^{3}s))
f - linear branching coefficient
g - linear termination coefficient
g_0 - coefficient of linear termination on soot particles
m_p - mass of a soot particle

The expression for the spontaneous origination rate of radical nuclei, n_0 is modified by Magnussen and in the last version of EDC the following expression is used [64]

$$n_0 = 1.08 a_0 f_{\mathrm{c}} Y_{\mathrm{fu}} e^{-\frac{E}{RT}} \tag{2.17}$$

where Y_{fu} is the mean concentration of fuel, and f_{c} is the mass fraction of carbon in the fuel. a_0 is a constant which is dependent on the soot particle diameter

$$d_p^3 a_0 = \text{constant} \tag{2.18}$$

with the value $a_0 = 12.5 \cdot 10^{36}$ for $d_p = 178.5$ Å.

Table 2.1: Constants in the EDC soot model.

a	$f-g$	g_0	b	E/R	ρ_s	d_p	a_0
10^5	10^2	10^{-15}	$8 \cdot 10^{-14}$	$9 \cdot 10^4$	2000	178.5 Å	$12.5 \cdot 10^{36}$

Soot is allowed to grow on the radical nuclei and the total rate of formation of soot particles can be expressed as [64]

$$\omega_{s,f,I} = \frac{m_p}{\rho}\frac{dS}{dt} = \left(m_p a - b\rho Y_s\right) Y_n \quad \left[\frac{\text{kg soot}}{\text{kg} \cdot \text{s}}\right] \tag{2.19}$$

where S is the concentration of soot particles (part./m^3) and a and b are model constants. The mass of a soot particle, m_p is given by

$$m_p = \frac{\pi}{6}\rho_s d_p^3 \tag{2.20}$$

All constants in the soot model are given in Tab 2.1.

The combustion rate of of nuclei and soot is assumed to be proportional to the combustion rate of fuel.

$$\omega^*_{n/s,c} = \omega^*_{fu}\frac{\widetilde{Y}_{n/s}}{\widetilde{Y}_{fu}} \tag{2.21}$$

Version II

The EDC soot model was originally developed for modelling turbulent acetylene diffusion flames. To make the model applicable to other fuels and a wider range of conditions, Magnussen and coworkers have developed a generalisation of the formation model [59]. This generalised version of the model is outlined below and will be referred to as version II.

The maximum amount of soot which can be formed in the Tesner model, $Y_{s,max}$, can be found by examining Eq. 2.19. The maximum amount of soot will occur when

$$\frac{dY_s}{dt} = \omega_{s,f} = \left(m_p a - b\rho Y_s\right) Y_n = 0 \tag{2.22}$$

which yields

$$Y_{\mathrm{s,max}} = \frac{am_{\mathrm{p}}}{b\rho} \tag{2.23}$$

This maximum level is given by the model parameters and the density. The idea in version II of the EDC soot model is to limit the maximum amount of soot formed by the amount of carbon available in the fuel present. By substituting the variable $Y_{\mathrm{s,max}}$ into the existing equations for nucleus and soot the equations take the form:

$$\omega_{\mathrm{n,f,II}} = \frac{n_0}{\rho} + (f-g)Y_{\mathrm{n}}\frac{Y_{\mathrm{s,max,1}}}{Y_{\mathrm{s,max,3}}} - \frac{g_0 a}{b}Y_{\mathrm{n}}\frac{Y_{\mathrm{s}}}{Y_{\mathrm{s,max,3}}} \tag{2.24}$$

$$\omega_{\mathrm{s,f,II}} = \rho b Y_{\mathrm{s,max,1}} Y_{\mathrm{n}}\left(1 - \frac{Y_{\mathrm{s}}}{Y_{\mathrm{s,max,2}}}\right) \tag{2.25}$$

where

$$Y_{\mathrm{s,max,1}} = f_c Y_{\mathrm{fu}} - Y_{\mathrm{s,0}} \tag{2.26}$$

$$Y_{\mathrm{s,max,2}} = f_c Y_{\mathrm{fu}} \tag{2.27}$$

$$Y_{\mathrm{s,max,3}} = Y_{\mathrm{s,max,2}} \tag{2.28}$$

To limit the nucleus formation when the amount of available carbon is decreasing, the linear branching term in the equation for formation of nucleus, Eq. 2.24, is multiplied by a limiting factor, $Y_{\mathrm{s,max,1}}/Y_{\mathrm{s,max,3}}$.

The soot combustion model in version II is unchanged from version I of the model.

2.2.2 Moss and Lindstedt

In this section two semi-empirical soot models are presented. One developed by Peter Lindstedt and co-workers [60, 23] and one by the research group around Barrie Moss [13]. Both models have been used in predictions of turbulent flames, but to our knowledge they have previously never been used in conjunction with

EDC. Both models use two transport equations. One for soot particle density (Y_N) and one for soot mass fraction (Y_s). The equations are coupled through an assumption of spherical particles which conform to a monodisperse size distribution. The models are based on the same physical foundation and account for nucleation, soot mass growth, agglomeration, and soot oxidation. To make it easier to compare the two models, they are written in the same form. The model by Moss is put into the framework used by Lindstedt. The only differences between the models are the model parameters and constants.

The source term in the equation for soot volume fraction (Y_s) and the equation for particle number density (Y_N) can be written as

$$\rho\omega_s = R_1 + R_2 - R_3 \qquad \left[\frac{\text{kg soot}}{\text{m}^3 \cdot \text{s}}\right] \tag{2.29}$$

$$\rho\omega_N = R_4 - R_5 \qquad \left[\frac{\text{particles}}{\text{m}^3 \cdot \text{s}}\right] \tag{2.30}$$

where R_i represents the different mechanisms in the model.

R_1 - nucleation
R_2 - soot mass formation
R_3 - soot oxidation
R_4 - nucleation
R_5 - agglomeration

The source term for nucleation (R_1) and soot mass growth (R_2) include a modified Arrhenius rate constant of the form $k_i = A_i T^{b_i} e^{-E_i/RT}$. The values of the different Arrhenius parameters and other model constants are given in Tab. 2.2.

The nucleation step is based on the following reaction step

$$C_2H_2 \rightarrow 2C_s + H_2 \tag{2.31}$$

The nucleation rate constant is now written

$$R_1 = 2k_1(T)\,[C_2H_2]\,M_s \tag{2.32}$$

where M_s is the molar mass of soot, 12.011 kg/kmol.

The source term in the particle number density equation due to nucleation is written

$$R_4 = \frac{2}{C_{\min}} N_A k_1(T) [C_2H_2] \tag{2.33}$$

where $C_{\min}$ is the number of carbon atoms in the incipient soot particle. N_A is Avogadro's number.

The soot particles are assumed to grow by adsorption of C_2H_2 on the surface of the particles

$$C_2H_2 + nC_s \rightarrow (n+2)C_s + H_2 \tag{2.34}$$

The soot mass growth is assumed to be first order in acetylene concentration.

$$R_2 = 2k_2(T) f(S) [C_2H_2] M_s \tag{2.35}$$

where $f(S)$ is a function of the soot surface areal. Assuming spherical particles the surface area is written

$$S = \pi d_p^2 \rho Y_N \tag{2.36}$$

and the particle diameter, d_p, is found from

$$d_p = \left(\frac{6}{\pi} \frac{Y_s}{\rho_s Y_N} \right)^{1/3} \tag{2.37}$$

The soot surface area may now be written

$$S = \pi \left(\frac{6}{\pi \rho_s Y_N} \right)^{2/3} Y_s^{2/3} \rho Y_N \tag{2.38}$$

How the soot mass growth depends on the available surface is uncertain. It is known from some experimental studies of premixed flames [38, 101] that the reactivity of the soot particles is reduced throughout the flame. One way to account for this aging effect is to assume that the number of active sites is proportional to the square root of the soot area available. Lindstedt has used this assumption in some of his work [56]. Brookes and Moss [13] analysed a turbulent methane-air

diffusion flame and found that the appropriate function is linear. In the present work $f(S)$ is simply set equal to S. This is in accordance with a similar work by Kronenburg et al. [53]

The soot mass growth step may now be written

$$\mathrm{R}_2 = k_2(T)\pi \left(\frac{6}{\pi\rho_\mathrm{s} Y_\mathrm{N}}\right)^{2/3} \rho Y_\mathrm{N}\, Y_\mathrm{s}^{1/3}\, [\mathrm{C_2H_2}]\, M_\mathrm{s} \tag{2.39}$$

Moss and Lindstedt include different species as oxidisers of soot. Moss uses OH as the oxidiser while Lindstedt originally includes only $\mathrm{O_2}$. OH is known to have a strong oxidising effect on soot and $\mathrm{O_2}$ is not adequate as the only soot oxidiser in the general case. Therefore, OH is included in the model by Lindstedt. Rate constants are taken from Bradley et al. [8]. This is the same model for OH oxidation used by Kronenburg et al. [53] in a similar study. The chemical model equations for soot oxidation are

$$\mathrm{C_s} + \frac{1}{2}\mathrm{O_2} \rightarrow \mathrm{CO} \tag{2.40}$$

$$\mathrm{C_s} + \mathrm{OH} \rightarrow \mathrm{CO} + \mathrm{H} \tag{2.41}$$

The soot oxidation term takes the form

$$\mathrm{R}_3 = k_3(T) S\, [\mathrm{O_2}]\, M_\mathrm{s} + k_6(T) S\, [\mathrm{OH}]\, M_\mathrm{s} \tag{2.42}$$

Agglomeration is modelled using a normal square dependence [98, 41]

$$\mathrm{R}_5 = 2C_a\sqrt{d_p}\left(\frac{6\kappa T}{\rho_\mathrm{s}}\right)^{1/2} (\rho Y_\mathrm{N})^2 \tag{2.43}$$

where C_a is the agglomeration rate constant. This expression, without the C_a-constant, is found from free-molecule kinetic theory. Measured values of the agglomeration rate have been found to be several times higher than the theoretical rate. The agglomeration constant has therefore been included. The value of this

Table 2.2: Constants in the soot models

	General		Nucleation				Mass growth		
	ρ_s	M_s	A_1	b_1	$\frac{E_1}{R}$	C_{min}	A_2	b_2	$\frac{E_2}{R}$
Lind.	2000	12.011	6300	0.0	21 100	100	750	0.0	12 100
Moss	1800	12.011	324	0.0	21 100	60	487	0.0	12 100

	Oxidation						Agglomeration
	A_{O_2}	b_{O_2}	$\frac{E_{O_2}}{R}$	A_{OH}	b_{OH}	$\frac{E_{OH}}{R}$	C_a
Lind.	715	0.5	19,680	0.36	0.5	0.0	9.0
Moss	0.0	0.0	0.0	0.35	0.5	0.0	1.0

constant differs in the literature. As can be seen from Table 2.2, Lindstedt uses a value of 9 while Moss uses the theoretical expression i.e. $C_a = 1$. Another common value for C_a in the literature is 3 [41]

By using Eq. 2.37 we get

$$R_5 = 2C_a \left(\frac{6}{\pi \rho_s Y_N}\right)^{1/6} \left(\frac{6\kappa T}{\rho_s}\right)^{1/2} Y_s^{1/6} (\rho Y_N)^2 \tag{2.44}$$

Chapter 3

Physical Fundamentals

In turbulent combustion a large number of different processes are taking place. These processes include physical transport mechanisms and chemical reactions. Many of the processes are linked to each other and this makes numerical simulation of turbulent combustion a complex task. In principle, all of these processes can be described by molecular considerations. However, to describe all occurring processes from a molecular viewpoint would lead to a overwhelming simulation task, even for the most powerful computers of today. Also, the underlying physics for some of the processes are not fully known and empirical data and models has to be used.

In this chapter the physical foundation for the models used in the present work is presented. All equations are presented in standard Cartesian tensor notation.

3.1 Properties of the Gas Mixture

To solve the conservation equations presented later in this chapter, properties that describe the gas mixture are needed.

For the operating conditions of the flames studied in the present work, the gas mixture can be assumed to behave as an ideal-gas mixture. This means that the temperature, density, and pressure of the mixture are related by the ideal-gas equation of state [74]

$$p = \rho \frac{R_u}{M} T \tag{3.1}$$

where M is the molecular mass of the mixture and is calculated as a mole-fraction average of the component molecular masses:

$$M = \sum_{k=1}^{n_s} X_k M_k \tag{3.2}$$

where X_k is the mole fraction of species k.

The enthalpy for an ideal-gas mixture is found from the enthalpy of the components.

$$h = \sum_{k=1}^{n_s} Y_k h_k \tag{3.3}$$

where Y_k is the mass fraction of species k. For an ideal-gas the enthalpy is an unique function of temperature, and the enthalpy at a given temperature is calculated from

$$h_k(T) = h_k^\circ + \int_{T^\circ}^{T} c_{p,k}(T) dT \tag{3.4}$$

where h_k° is the specific enthalpy of formation at a reference temperature T°, and $c_{p,k}(T)$ is the specific heat capacity at constant pressure for the same species.

$$c_{p,k} = \left(\frac{\partial h}{\partial T} \right)_p \tag{3.5}$$

In the present work, $h_k(T)$ and $c_{p,k}(T)$ are calculated using the Chemkin II [49] software package together with thermodynamic data from the chemical reaction mechanism GRI-Mech 2.11 [7].

3.2 Molecular Transport

In laminar flow all transport processes except for the bulk transport and radiation takes place on a molecular level. In turbulent flow, the transport is enhanced by the turbulent fluctuations. In most turbulent flows, the transport due to the turbulent fluctuations, is much stronger than the molecular transport and, if the turbulence is intense, molecular transport can be neglected. Due to this difference in strength between the transport mechanisms, and the fact that the focus of the present work is turbulent combustion, simplified expressions can be used to model the molecular transport.

3.2.1 Momentum Flux

In laminar flow, the molecular transport of momentum is dependent on the molecular viscosity, μ, of the fluid. The viscous stress tensor represents the molecular flux of momentum in the flow. For a Newtonian fluid, this is given by [4]

$$\tau_{kj} = \mu \left(\frac{\partial v_k}{\partial x_j} + \frac{\partial v_j}{\partial x_k} \right) + \left(\mu_B - \frac{2}{3}\mu \right) \frac{\partial v_l}{\partial x_l} \delta_{kj} \tag{3.6}$$

where μ_B is called the bulk viscosity and expresses the resistance of the fluid against rapid changes in volume. In the present work $\mu_B = 0$ has been used. This is known as the Stokes-hypothesis. The correctness of this hypothesis has been questioned by by several scientists but in lack of better value of μ_B, employment of the Stokes-hypothesis has become the usual practice.

The viscous stress tensor may also be interpreted as the viscous force on a fluid element.

The viscosity of a pure species (μ_k) is a function of temperature and can be calculated from kinetic theory [43]. In the present work, the calculation routines in the CHEMKIN II [49] transport package has been used to compute μ_k. The viscosity of the mixture is found by the relation [78]

$$\mu = \frac{\sum_{k=1}^{n_s} Y_k \mu_k \sqrt{M_k}}{\sum_{k=1}^{n_s} Y_k \sqrt{M_k}} \tag{3.7}$$

3.2.2 Mass Flux

The molecular mass flux of species k in the x_j direction, j_j^k, generally has three components. These are known as mass diffusion, pressure diffusion, and thermal diffusion (Soret effect) [43]. For most combustion processes, the pressure diffusion and Soret effect may be neglected [97] and this practice has been adapted in the present work. The diffusion flux of species k in the j-direction is given by Fick's law

$$-j_j^k = \rho D \frac{\partial Y_k}{\partial x_j} \tag{3.8}$$

The diffusion coefficient D will be be different for different species, and it will be a function of the concentrations of all other species in the mixture. Because the focus of the present work is on turbulent flames, the simplification is made that all species have the same diffusion coefficient. As explained earlier, in most turbulent flows, turbulent transport will dominate. The turbulent fluctuations also make it necessary to treat the conservation equations in a statistical manner, and the resulting equations are simplified if a single diffusion coefficient is used. Also, the turbulent combustion models which are available today become rather complex if species-dependent diffusion coefficients are used.

The description of mass flux is further simplified by introducing the non-dimensional Schmidt number

$$\sigma_y = \frac{\mu}{\rho D} \tag{3.9}$$

The mass flux may now be expressed by the viscosity and Schmidt number

$$-j_j^k = \frac{\mu}{\sigma_y} \frac{\partial Y_k}{\partial x_j} \tag{3.10}$$

3.2.3 Energy Flux

the thermal energy flux can be divided into three components.

$$j_j^q = (j_c^q)_j + (j_d^q)_j + (j_D^q)_j \tag{3.11}$$

where $(j_c^q)_j$ is energy flux due to conduction, $(j_d^q)_j$ is energy flux due to species diffusion, and $(j_D^q)_j$ is energy flux due to concentration gradients, the Dufor-effect, all in the x_j direction. The latter of these components, the Dufor-effect is usually much smaller than the other two components [4], and has been neglected in the present work.

The energy flux due to conduction is expressed by Fourier's law

$$-(j_c^q)_j = \lambda \frac{\partial T}{\partial x_j} \tag{3.12}$$

with λ being the thermal conductivity. In the following section a conservation equation for energy is presented in which the energy flux is included. Consequently, it is desirable to express the energy flux due to conduction as a function of enthalpy instead of temperature. The following expression is obtained by combining Eqs. 3.3, 3.4, and 3.5

$$(j_c^q)_j = \frac{\lambda}{c_p}\left(\sum_{k=1}^{n_s} h_k \frac{\partial Y_k}{\partial x_j} - \frac{\partial h}{\partial x_j}\right) \tag{3.13}$$

Energy flux due to diffusion occurs, as indicated by the name, due to diffusion of species with different enthalpy and can be expressed by

$$(j_d^q)_j = \sum_{i=k}^{n_s} h_k j_j^k \tag{3.14}$$

Similar to the introduction of the Schmidt number in the section on mass flux, the non-dimensional Prandtl number (σ) is introduced to simplify the description of energy flux

$$\sigma = \frac{\mu c_p}{\lambda} \tag{3.15}$$

The Lewis number (Le) is the ratio of the Schmidt and Prandtl numbers

$$\mathrm{Le} = \frac{\sigma_y}{\sigma} \tag{3.16}$$

By introducing Eqs. 3.10, 3.15, and 3.16 into Eqs. 3.13 and 3.14, the total energy flux may be written

$$j_j^q = \frac{\mu}{\sigma}\left[-\frac{\partial h}{\partial x_j} + \left(1 - \frac{1}{\mathrm{Le}}\right)\sum_{k=1}^{n_s}\frac{\partial Y_k}{\partial x_j}\right] \tag{3.17}$$

For most gases the Lewis number is close to unity [54] and by assuming Le=1 the expression for the energy flux is further simplified.

3.3 Conservation Equations

To describe turbulent combustion mathematically, a set of partial differential equations are used as a basis. These differential equations are statements of conservation of the fundamental properties mass, momentum and energy in the system. The equations are presented in standard Cartesian tensor notation.

3.3.1 Conservation of Mass

The conservation equation for a single species k expressed by its mass fraction Y_k, is [4, 20]

$$\frac{\partial}{\partial t}\left(\rho Y_k\right) + \frac{\partial}{\partial x_j}\left(\rho Y_k v_j\right) = \frac{\partial}{\partial x_j}\left(-j_j^k\right) + \rho\omega_k \tag{3.18}$$

where ρ is the density and v_j is the velocity in the x_j direction. The first term in the equation is the time rate change of the concentration of species k per volume. The second term represents the convective transport of the same species. The last term of the equation ($\rho\omega_k$) is the net production rate of species k due to chemical reactions. The term $-j_j^k$ represents the diffusion flux of species k in the j-direction given by Fick's law, Eq. 3.8. By introducing the Schmidt number (Eq. 3.9), and assuming a Lewis number (Eq. 3.16) of unit,y the conservation of species k can be written as

$$\frac{\partial}{\partial t}\left(\rho Y_k\right) + \frac{\partial}{\partial x_j}\left(\rho Y_k v_j\right) = \frac{\partial}{\partial x_j}\left(\frac{\mu}{\sigma}\frac{\partial Y_k}{\partial x_j}\right) + \rho\omega_k \tag{3.19}$$

By summing up the conservation equations for all the species the conservation equation for overall mass appears. This equation is usually called the continuity equation [4]

$$\frac{\partial \rho}{\partial t} + \frac{\partial}{\partial x_j}\left(\rho v_j\right) = 0 \tag{3.20}$$

3.3.2 Conservation of Momentum

The velocity field of the system is determined by the forces acting on the system. Newton's second law of motion relates the sum of all forces acting on the system and the linear momentum of the system

$$\sum F_j = \frac{D\left(m v_j\right)}{Dt} \tag{3.21}$$

where the operator D/Dt is the substantial or material derivative. By applying Newton's second law to an infinitesimal control volume fixed in space, the conservation equation for linear momentum may be derived [4, 20, 99].

$$\frac{\partial}{\partial t}\left(\rho v_k\right) + \frac{\partial}{\partial x_j}\left(\rho v_k v_j\right) = -\frac{\partial p}{\partial x_k} + \frac{\partial}{\partial x_j}\left(\tau_{kj}\right) + \rho b_k \tag{3.22}$$

where τ_{kj} is the viscous stress tensor and is given by Eq. 3.6.

3.3.3 Conservation of Energy

The first law of thermodynamics states that the total energy of a system and its surroundings is conserved. For an open system this principle can be expressed by the following equation [4, 20, 54]

$$\frac{\partial}{\partial t}\left(\rho e_t\right) + \frac{\partial}{\partial x_j}\left(\rho e_t v_j\right) = -\frac{\partial j_j^q}{\partial x_j} + Q - \frac{\partial}{\partial x_j}\left(p v_j\right) + \frac{\partial}{\partial x_j}\left(\tau_{ij} u_i\right), \tag{3.23}$$

where e_t is the total energy of the fluid. The total energy e_t is the sum of the internal energy (u), potential energy (ϕ), and kinetic energy ($1/2 v_i v_i$). j_j^q is the thermal

energy flux in the x_j direction and Q is the internal production rate of thermal energy, for example due to radiation. The two last terms in Eq. 3.23 represent work done on the fluid by pressure forces and viscous forces respectively.

In numerical simulations of turbulent combustion, it is often desirable to use an equation for temperature or enthalpy instead of the total energy. In the present case an equation for enthalpy (h) has been used. A conservation equation for the enthalpy may be derived from the first law of thermodynamics in several ways. The enthalpy is linked to the internal energy by its definition

$$h = u + \frac{p}{\rho}. \tag{3.24}$$

By subtracting equations for the kinetic and potential energy from Eq. 3.23 an equation for the internal energy is found. The conservation equation for kinetic energy may be found by multiplying the conservation equation of linear momentum (Eq. 3.22) with v_i, resulting in

$$\frac{\partial}{\partial t}\left(\rho\frac{1}{2}v_i v_i\right) + \frac{\partial}{\partial x_j}\left(\rho\frac{1}{2}v_i v_i v_j\right) = -v_i\frac{\partial p}{\partial x_i} + v_i\frac{\partial \tau_{ij}}{\partial x_j} + \rho v_j b_j \tag{3.25}$$

An equation for the potential energy is found by multiplying the equation of continuity (Eq. 3.20) with the stationary potential Φ defined as

$$b_j = -\frac{\partial \Phi}{\partial x_j} \tag{3.26}$$

The following equation is obtained

$$\frac{\partial}{\partial t}\left(\rho\Phi\right) + \frac{\partial}{\partial x_j}\left(\rho\Phi v_j\right) = -\rho v_j b_j \tag{3.27}$$

By subtracting Eqs. 3.25 and 3.27 from Eq. 3.23 and using the definition of enthalpy (Eq. 3.24) the conservation equation for enthalpy is finally obtained.

$$\frac{\partial}{\partial t}\left(\rho h\right) + \frac{\partial}{\partial x_j}\left(\rho h v_j\right) = \frac{\partial p}{\partial t} + v_j\frac{\partial p}{\partial x_j} - \frac{\partial j_j^q}{\partial x_j} + \tau_{ij}\frac{\partial v_i}{\partial x_j} + Q \tag{3.28}$$

The molecular (j_j^q) energy flux is given by Eq. 3.17 where Le=1 is assumed. The equation is further simplified by neglecting the terms $v_j \partial p/\partial x_j$ and $\tau_{ij}\partial v_i/\partial x_j$. This assumption is justified as long as there are no extreme pressure gradients occurring in the system [97]. These assumptions lead to the simplified energy equation

$$\frac{\partial}{\partial t}(\rho h) + \frac{\partial}{\partial x_j}\left(\rho h v_j\right) = \frac{\partial p}{\partial t} + \frac{\partial}{\partial x_j}\left(\frac{\mu}{\sigma}\frac{\partial h}{\partial x_j}\right) + Q \tag{3.29}$$

3.3.4 The General Transport Equation

By inspection of the conservation equations it is apparent that they have a similar form. Due to this similarity, basically the same numerical procedure can be followed to solve all the conservation equations. The equations can be represented by a general transport equation.

$$\frac{\partial}{\partial t}(\rho\phi_i) + \frac{\partial}{\partial x_j}\left(\rho\phi_i v_j\right) = \frac{\partial}{\partial x_j}\left(\Gamma_i \frac{\partial \phi_i}{\partial x_j}\right) + S_i \tag{3.30}$$

where ϕ_i represents a scalar variable, for example v_j or h, while Γ_i and S_i are the corresponding diffusion coefficient and source term, respectively.

3.4 Chemical Kinetics

The source term ω_k in Eq. 3.19 represents the net production rate of species k due to chemical reactions. In gaseous combustion this reaction rate is found by using an appropriate reaction mechanism. This reaction mechanism consists of a set of elementary reactions with corresponding rate parameters. If the reaction mechanism consist of n_s species and n_cr chemical reactions, an arbitrary reaction in the reaction mechanism can be expressed as [54, 97]

$$\sum_{i=1}^{n_\mathrm{s}} \nu'_{il} A_i \longrightarrow \sum_{i=1}^{n_\mathrm{s}} \nu''_{il} A_i \qquad l = 1, \ldots, n_\mathrm{cr} \tag{3.31}$$

where ν'_{il} and ν''_{il} are the stoichiometric coefficients of reactants or products of species i in reaction l and A_i is the specification of species i.

The chemical production rate for species i is now expressed as [97]

$$\omega_i = \frac{M_i}{\rho} \sum_{l=1}^{n_{\mathrm{cr}}} k_l \left(\nu''_{il} - \nu'_{il}\right) \prod_{k=1}^{n_{\mathrm{s}}} c_k^{\nu'_{il}} \tag{3.32}$$

with c_k being the concentration of species k. k_l is the rate coefficient for reaction l and is calculated from a modified Arrhenius expression

$$k_l = A_l T^{b_l} \exp\left(\frac{E_{a,l}}{R_u T}\right) \tag{3.33}$$

where A_l is the preexponential factor, b_l is the temperature exponent and $E_{a,l}$ is the activation energy. These rate parameters, together with the selection of elementary reactions and their stoichiometric coefficients, constitute the reaction mechanism.

3.5 Radiation

Thermal radiation may have a large influence upon the combustion process. Energy will be transfered from the high temperature gas mixture to its cooler surroundings by thermal radiation. This transfer of energy will lead to a lower combustion temperature. The energy transfer due to radiation is represented by a source term in the energy equation (Eq. 3.29). The amount of energy being transfered to the surroundings depends on the gas temperature as well as the composition of the burning gas mixture.

Particularly, if soot particles are present in the combustion gas mixture, they will greatly enhance radiation from the flame. Thermal radiation from soot has a major influence on peak temperatures in the flame. Soot formation and oxidation are highly influenced by the temperature, and it is therefore necessary to account for radiation in the simulations.

In the present predictions, a simple radiation model has been employed where only emission from the flame is included. The flame is assumed to be optical thin, such that each radiating point source has an unlimited isotropic view of the cold surroundings. This means that emitted energy from the gas passes within the system without significant attenuation. Furthermore, energy incident from the boundaries is neglected. The model includes radiation from the species CO_2, H_2O, CH_4, and CO in addition to soot.

The emitted energy from an isothermal volume with only spontaneous emission is found by integrating the spectral emissive power over all wavelengths (λ) [45, 89]

$$Q_{\text{emi}} = 4 \int_0^\infty a_\lambda \left(\lambda, T, p\right) E_{\lambda,b} \left(\lambda, T\right) d\lambda \tag{3.34}$$

where a_λ is the absorption coefficient of the medium. $E_{\lambda,b}$ is the spectral emissive power from a perfect (black body) radiator and is given by the Planck distribution [46, 89]

$$E_{\lambda,b} = \frac{C_1}{\lambda^5 \left[\exp\left(\frac{C_2}{\lambda T}\right) - 1\right]} \tag{3.35}$$

where the two radiation constants are $C_1 = 2\pi h c_0^2$ and $C_2 = h c_0 / k$. Here, h and k are the universal Planck and Boltzmann constants, respectively, and c_0 is the speed of light in vacuum.

The Planck mean absorption coefficient, $a_P(T, p)$, is defined as [89]

$$a_P(T, p) = \frac{\int_0^\infty a_\lambda \left(\lambda, T, p\right) E_{\lambda,b} \left(\lambda, T\right) d\lambda}{\int_0^\infty E_{\lambda,b} \left(\lambda, T\right) d\lambda} \tag{3.36}$$

where the denominator can be integrated to give

$$a_P(T, p) = \frac{\int_0^\infty a_\lambda \left(\lambda, T, p\right) E_{\lambda,b} \left(\lambda, T\right) d\lambda}{\sigma T^4} \tag{3.37}$$

with σ being the Stefan-Boltzmann constant.

If the Planck mean absorption coefficient is known, the emitted power from the volume can be readily calculated by combining Eqs. 3.37 and 3.34

$$Q_{\text{emi}} = 4 a_P(T, p) \sigma T^4 \tag{3.38}$$

To calculate radiation from the gas phase species, Planck mean absorption coefficients suggested by the International Workshop on Measurement and Computation of Turbulent Non-premixed Flames [3, 90] has been used. The total absorption coefficient for the gas is given by

$$a_{P,\text{gas phase}} = \sum_i p_i a_{P,i} \tag{3.39}$$

where $a_{P,i}$ is the Planck mean absorption coefficient of species i, and p_i is the partial pressure of species i. Suggested expressions for $a_{P,i}$ for the gas-phase species considered are given in [90] as functions of temperature and these expressions have been used in the present work.

The absorption coefficient for soot particles used in the present work is found from experimental data. R. J. Hall analysed results from Mie-scattering measurements in diffusion flames and used the following expression for the absorption coefficient of soot particles [37]

$$a_{\lambda,\text{S}} = \frac{C_{\lambda,0} f_v}{\lambda} \tag{3.40}$$

where f_v is the volume fraction of soot and C_λ is a constant. By introducing this expression into Eq. 3.34 and performing the integration, the emitted energy from soot in the volume can be expressed as [37]

$$Q_{\text{soot}} = 4 C_\lambda \sigma f_v T^5 \tag{3.41}$$

where the constant C_λ has the value 1.307×10^3 $\text{m}^{-1}\text{K}^{-1}$.

The total energy emitted from the volume is now found from.

$$Q_{\text{emi}} = 4\sigma \left[\left(T^4 - T_b^4\right) \sum_i p_i a_{P,i} + C_\lambda f_v \left(T^5 - T_b^5\right) \right] \tag{3.42}$$

where T_b is the temperature of the cold surroundings. The subtractions of T_b^4 and T_b^5 in Eq. 3.42 are not consistent with the emission-only model. However, these terms are included to avoid the unphysical possibility of calculated temperatures in the Co-flowing air dropping below the ambient temperature. The effect of the T_b terms on the calculated flames is negligible [3, 90].

Chapter 4

Modelling of Turbulent Combustion

4.1 Introduction

The nature of turbulent flow is irregular with rapid fluctuations in velocity, density, temperature, and composition. This fluctuating nature makes turbulent flow highly diffusive resulting in enhanced transport of momentum, mass, and energy. The basic physics of these transport mechanisms is the same as for laminar flow, and the expressions for molecular transport presented in the previous chapter, are still valid for turbulent flow. If the turbulence levels are moderate, the transport equations (cf. Sec. 3.3) can be solved to yield the instantaneous values for velocity, temperature and composition. This is called direct numerical simulation (DNS). However, in most practical turbulent flows, the task of resolving the fluctuations would require extremely fine grids and high time resolution. Even for modern computers this would be an impracticable task. An approach to reduce the computational task is to apply a statistical treatment of the transport equations. The instantaneous variables are decomposed into a mean and a fluctuation. Instead of solving transport equations for instantaneous quantities, transport equations for

mean quantities are solved. This approach requires turbulence models which relates the mean quantities to the turbulence fluctuations.

The introduction of mean quantities makes the numerical handling of turbulent flow simpler. However, it also causes new challenges, especially related to the handling of chemical kinetics. The source terms in the Favre-averaged transport equations for the individual species are exponential functions of temperature (cf. Eqs. 3.32 and 3.33). Using the mean temperature to compute a mean source term will lead to an erroneous result. Accordingly, the averaged chemical production rates need special treatment and are approximated by a combustion model.

4.2 Favre-Averaged Conservation Equations

To average the equations the instantaneous variables are decomposed into a mean and a fluctuation.

$$\varphi = \overline{\varphi} + \varphi', \tag{4.1}$$

where $\overline{\varphi}$ is the mean and φ' the fluctuation. When modelling turbulent flows with a varying density such as turbulent combustion, it is often favourable to use density-weighted means [20]

$$\varphi = \widetilde{\varphi} + \varphi'', \tag{4.2}$$

where $\widetilde{\varphi}$ is the density-weighted mean defined as

$$\widetilde{\varphi} = \frac{\overline{\rho\varphi}}{\bar{\rho}}. \tag{4.3}$$

By introducing Eq. 4.2 into the conservation equations (cf. Sec 3.3) and perform the averaging, the Favre-averaged conservation equations are obtained:

Mass conservation of species k

$$\frac{\partial}{\partial t}\left(\bar{\rho}\widetilde{Y}_k\right) + \frac{\partial}{\partial x_j}\left(\bar{\rho}\widetilde{Y}_k\tilde{v}_j\right) = \frac{\partial}{\partial x_j}\left(\frac{\mu}{\sigma}\frac{\partial \widetilde{Y}_k}{\partial x_j} - \bar{\rho}\widetilde{Y_k''v_j''}\right) + \bar{\rho}\widetilde{\omega}_k. \tag{4.4}$$

Conservation of overall mass

$$\frac{\partial \bar{\rho}}{\partial t} + \frac{\partial}{\partial x_j}\left(\bar{\rho}\tilde{v}_j\right) = 0. \tag{4.5}$$

Conservation of momentum

$$\frac{\partial}{\partial t}\left(\bar{\rho}\tilde{v}_k\right) + \frac{\partial}{\partial x_j}\left(\bar{\rho}\tilde{v}_k\tilde{v}_j\right) = -\frac{\partial \bar{p}}{\partial x_k} + \frac{\partial}{\partial x_j}\left(\overline{\tau}_{kj} - \bar{\rho}\widetilde{v_k''v_j''}\right) + \bar{\rho}\tilde{b}_k. \tag{4.6}$$

Conservation of energy

$$\frac{\partial}{\partial t}\left(\bar{\rho}\tilde{h}\right) + \frac{\partial}{\partial x_j}\left(\bar{\rho}\tilde{h}\tilde{v}_j\right) = \frac{\partial \bar{p}}{\partial t} + \frac{\partial}{\partial x_j}\left(\frac{\mu}{\sigma}\frac{\partial \tilde{h}}{\partial x_j} - \bar{\rho}\widetilde{h''v_j''}\right) + \bar{\rho}\,\widetilde{Q}. \tag{4.7}$$

Conservation of a general scalar variable ϕ_i

$$\frac{\partial}{\partial t}\left(\bar{\rho}\tilde{\phi}_i\right) + \frac{\partial}{\partial x_j}\left(\bar{\rho}\tilde{\phi}_i\tilde{v}_j\right) = \frac{\partial}{\partial x_j}\left(\Gamma_i\frac{\partial \tilde{\phi}_i}{\partial x_j} - \bar{\rho}\widetilde{\phi_i''v_j''}\right) + \overline{S}_i. \tag{4.8}$$

Compared to the equations for the instantaneous variables presented in Sec. 3.3, several new terms have appeared due to the averaging. These new terms are known as turbulence stresses $-\bar{\rho}\widetilde{v_k''v_j''}$, and turbulence fluxes $-\bar{\rho}\widetilde{Y_k''v_j''}$, $-\bar{\rho}\widetilde{h''v_j''}$, and $-\bar{\rho}\widetilde{\phi_i''v_j''}$. These terms are unknown and to make it possible to solve the averaged conservation equations, they have to be approximated in some way. Methods for for approximating these unknown terms are called turbulence models. A large number of turbulence models have been developed. However, for simulating turbulent combustion there are mainly two different types of models which are in use at present. The most commonly used model today is the k-ε-model, and this model has also been used in the present work. In addition, a class of models called Reynolds-Stress-Equation (RSE) models are frequently being used.

4.3 k-ε turbulence model

As described Sec. 4.1, turbulence will enhance transport in the flow. The k-ε-model was presented by Jones and Launder [47] and is based on the assumption that the turbulent transport can be described by using an effective viscosity

$$\mu_{\text{eff}} = \mu + \mu_{\text{t}}, \tag{4.9}$$

where μ_{t} is the eddy (or turbulence) viscosity. The turbulence stresses are now expressed by the eddy viscosity from an analogy with the expression for viscous stresses (Eq. 3.6) [20]

$$-\bar{\rho}\widetilde{v_k'' v_j''} = \mu_{\text{t}} \left(\frac{\partial \tilde{v}_k}{\partial x_j} + \frac{\partial \tilde{v}_j}{\partial x_k} \right) - \frac{2}{3} \left(\bar{\rho}\tilde{k} + \mu_{\text{t}} \frac{\partial \tilde{v}_l}{\partial x_l} \right) \delta_{kj}, \tag{4.10}$$

where $\tilde{k}$ is the turbulence kinetic energy and is described below. The turbulence fluxes are modelled in analogy with the molecular fluxes, cf. Eqs. 3.10 and 3.17. For a general scalar variable the turbulent flux is expressed as [20]

$$-\bar{\rho}\widetilde{\phi_i'' v_j''} = \frac{\mu_{\text{t}}}{\sigma_{\text{t}}} \frac{\partial \tilde{\varphi}_i}{\partial x_j} \tag{4.11}$$

where σ_{t} is the turbulence Prandtl-Schmidt number.

To complete the model it is necessary to know the variables μ_{t}, σ_{t}, and k. The turbulence kinetic energy is defined as

$$\tilde{k} = \frac{1}{2}\widetilde{v_l'' v_l''}. \tag{4.12}$$

By the aid of the instantaneous and the Favre-averaged momentum equations, a transport equation for $\tilde{k}$ can be obtained [20]. However, in this transport equation there are several terms which has to be modelled. In the present work the modelled equation suggested by Jones and Launder [47] has been used

$$\frac{\partial}{\partial t}\left(\bar{\rho}\tilde{k}\right) + \frac{\partial}{\partial x_j}\left(\bar{\rho}\tilde{k}\tilde{v}_j\right) = \frac{\partial}{\partial x_j}\left[\left(\mu + \frac{\mu_{\text{t}}}{\sigma_k}\right)\frac{\partial \tilde{k}}{\partial x_j}\right] + \bar{\rho}P_k - \bar{\rho}\tilde{\varepsilon}. \tag{4.13}$$

Table 4.1: Constants in the k-ε model [55].

σ_t	σ_k	σ_ε	$C_{\varepsilon 1}$	$C_{\varepsilon 2}$	C_μ
0.7	1.0	1.3	1.44	1.92	0.09

The variable $\tilde{\varepsilon}$ represents the dissipation of turbulence energy into heat. The dissipation of turbulence energy is found from a modelled transport equation

$$\frac{\partial}{\partial t}\left(\bar{\rho}\tilde{\varepsilon}\right) + \frac{\partial}{\partial x_j}\left(\bar{\rho}\tilde{\varepsilon}\tilde{v}_j\right) = \frac{\partial}{\partial x_j}\left[\left(\mu + \frac{\mu_\mathrm{t}}{\sigma_\varepsilon}\right)\frac{\partial \tilde{\varepsilon}}{\partial x_j}\right] + C_{\varepsilon 1}\frac{\tilde{\varepsilon}}{\tilde{k}}\bar{\rho}P_k - C_{\varepsilon 2}\frac{\tilde{\varepsilon}}{\tilde{k}}\bar{\rho}\tilde{\varepsilon}. \quad (4.14)$$

The term P_k present in the two transport equations, is the production of turbulence kinetic energy [20, 47]

$$\bar{\rho}P_k = \mu_\mathrm{t}\left(\frac{\partial \tilde{v}_k}{\partial x_j} + \frac{\partial \tilde{v}_j}{\partial x_k}\right)\frac{\partial \tilde{v}_k}{\partial x_j} - \frac{2}{3}\left(\bar{\rho}\tilde{k} + \mu_\mathrm{t}\frac{\partial \tilde{v}_l}{\partial x_l}\right)\frac{\partial \tilde{v}_j}{\partial x_j}. \quad (4.15)$$

The eddy viscosity is expressed as

$$\mu_\mathrm{t} = C_\mu \bar{\rho}\frac{\widetilde{k^2}}{\tilde{\varepsilon}}. \quad (4.16)$$

The parameters σ_t, σ_k, σ_ε, $C_{\varepsilon 1}$, $C_{\varepsilon 2}$, and C_μ are model constants. In the present work, the values suggested by Launder and Spalding [55] have been used, cf. Tab. 4.1. The k-ε model is now complete and the unknown turbulence stresses and turbulence fluxes can be found from Eqs. 4.10 and 4.11 once the transport equations for $\tilde{k}$ and $\tilde{\varepsilon}$ have been solved.

The standard k-ε model presented above, has been used in simulations of a variety of different turbulent flows, usually yielding good results. However, the model is known to over-predict turbulence diffusion of round jets [87]. Pope [80] argues that there is a correlation between the mean straining of mean vorticity and the mean straining of turbulent vorticity. This straining of turbulent vorticity leads to greater scale reduction, greater dissipation, and a lower turbulent viscosity. This effect is not present in a two-dimensional flow because the mean vorticity vector is normal to the plane of the flow and no vortex stretching can take place. However,

in an axisymmetric jet, rings of vorticity are stretched as the jet is spread. To remedy this shortcoming in the standard k-ε model, Pope suggested to include an additional source term in the transport equation for dissipation of turbulence energy when simulating axisymmetric jets [80]

$$S_\varepsilon = \bar{\rho}\frac{\widetilde{k^2}}{\varepsilon}C_{\varepsilon 3}\frac{1}{4}\left(\frac{\partial \tilde{u}}{\partial r} - \frac{\partial \tilde{v}}{\partial x}\right)\frac{\tilde{v}}{r}, \tag{4.17}$$

where $C_{\varepsilon 3}$ is a model constant with a value of 0.8. Also, u and v are the velocity components in the axial and radial direction respectively, and r is the coordinate in the radial direction. All predictions presented later in this thesis are of axisymmetric jets, and it was found that predictions including this additional source term resulted in a better description of turbulent diffusion than the standard model.

4.4 Eddy Dissipation Concept

The combustion model used in this work is the Eddy Dissipation Concept (EDC). This was developed by Magnussen and Hjertager [65] and has later been extended by Magnussen [63, 64] and Gran [34]. EDC is based on the assumption that the chemical reactions occur in the regions where the dissipation of turbulence energy takes place.

4.4.1 The Energy Cascade

For combustion to occur, it is necessary for the reactant species to be mixed on a molecular level. In addition, some hot products must be present to ignite the mixture. This molecular mixing occurs when the turbulent eddies break up and their kinetic energy (turbulence energy) dissipates into heat. The regions of the flow where this dissipation takes place is called “fine structures”. To find the amount of fine structures in the flow, Magnussen uses an energy cascade model. In turbulent flow, eddies of different sizes and with different mechanical energy will be present. There will be a continuous spectrum of eddies ranging from the

largest eddies with low characteristic frequency to the smallest eddies with high characteristic frequency. This continuous spectre can be modelled by a cascade of discrete levels [20, 21, 93]. Large eddies are fuelled with mechanical energy from the mean flow. These large eddies will accelerate surrounding fluid into smaller eddies. Large eddies will also decrease in size and loose energy due to strain and stretching. In the cascade, eddies of a certain size is mainly generated from eddies at the next larger level in the cascade. This goes on to the smallest scale level, where the viscous forces are equal to the inertial forces. Smaller eddies will break up and the mechanical energy will dissipate into heat. At all levels in the cascade some of the mechanical energy is dissipated into heat. However, most of the dissipation takes place at the smaller scales in the cascade.

Magnussen [21, 63] uses a cascade where the characteristic frequency of the eddies is doubled from one level to the subsequent lower level. This creates a link between the smallest eddies, the fine structures, and the largest eddies in the cascade. By using this cascade model, characteristic scales for the fine structures are expressed as functions of the turbulence kinetic energy ($\tilde{k}$), the dissipation of turbulence kinetic energy ($\tilde{\varepsilon}$), and the molecular kinematic viscosity (ν). The expressions for the characteristic length scale and velocity scale for the fine structures are [21, 64]

$$L^* = \frac{2}{3}\left(\frac{3C_{\mathrm{D2}}^3}{C_{\mathrm{D1}}^2}\right)^{1/4}\left(\frac{\nu^3}{\tilde{\varepsilon}}\right)^{1/4} \tag{4.18}$$

$$u^* = \left(\frac{C_{\mathrm{D2}}}{3C_{\mathrm{D1}}^2}\right)^{1/4}(\nu\tilde{\varepsilon})^{1/4} \tag{4.19}$$

where $C_{\mathrm{D1}} = 0.134$ and $C_{\mathrm{D1}} = 0.5$ are model constants. These scales are of the same order of magnitude as the Kolmogorov scales.

Characteristic scales for the large eddies, the integral scales of the turbulence, are modelled by estimating the dissipation of turbulence energy using the integral scales for length and velocity

$$\tilde{\varepsilon} = \frac{3}{2}C_{\mathrm{D1}}\frac{u'^3}{L'}. \tag{4.20}$$

Such an estimate for $\tilde{\varepsilon}$ in the inertial range of the turbulence energy spectre is in accordance with the earlier works of Prandtl [81] and Tennekes and Lumley [93]. A relation between L' and u' is found by estimating the kinematic turbulence viscosity as a product of these two integral scales

$$\nu_t = \frac{\mu_t}{\rho} = L'u'. \tag{4.21}$$

These representative scales for the large and smallest eddies of the flow are now used to model some important variables in the combustion model.

It is assumed that the fine structures are located in regions between larger eddies and that the fine structures will tend to gather together in such regions [64]. The mass fraction of such fine structure regions is expressed as

$$\gamma_\lambda = \frac{u^*}{u'} = 2.1 \left(\frac{\nu \tilde{\varepsilon}}{\tilde{k}^2} \right)^{1/4}. \tag{4.22}$$

The mass fraction of fine structures in the flow is modelled as

$$\gamma^* = \gamma_\lambda^3. \tag{4.23}$$

The mass exchange rate between the fine structures and surroundings, divided by the fine structure mass, is modelled as

$$\dot{m}^* = 2\frac{u^*}{L^*} = 2.5 \left(\frac{\tilde{\varepsilon}}{\nu} \right)^{1/2}. \tag{4.24}$$

It is convenient to use the mass exchange rate divided by total mass, and this is given by

$$\dot{m} = \gamma^* \dot{m}^* \tag{4.25}$$

The numbers which appear in Eqs. 4.22 and 4.24 are combinations of the two model constants C_{D1} and C_{D2}, and no new constants have been introduced. However, for simplicity, the full model expressions have been omitted.

The EDC assumes that the fluid state is determined by the fine structure state, the surrounding state and the fraction of fine structures. The mass average of a variable can be found from the fine structure value and the surrounding value

$$\widetilde{\phi} = \gamma^* \chi \phi^* + \left(1 - \gamma^* \chi\right) \phi^\circ \tag{4.26}$$

where χ is the fraction of fine structures where reaction occurs. Expressions for χ will be discussed later.

4.4.2 The Reactor Model

As explained above, the chemical reactions are assumed to take place in the fine structures of the turbulent flow. The fine structures are assumed to behave as homogeneous, constant pressure reactors, see Fig. 4.1.

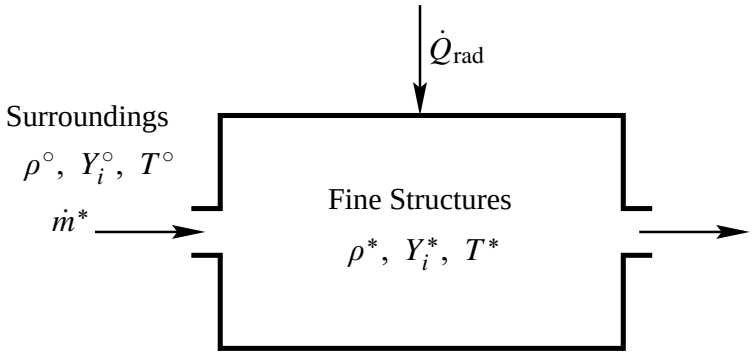

Figure 4.1: The fine structure is modelled as a homogeneous reactor.

The state of such a homogeneous reactor is determined by the following set of differential equations

$$\begin{aligned}
\frac{dp}{dt} &= 0 \\
\frac{dh^*}{dt} &= \dot{m}^* \left(h^\circ - h^*\right) + Q^*_{\text{rad}} \qquad \left[\frac{\text{J}}{\text{kg fine structure} \cdot \text{s}}\right] \\
\frac{dY_i^*}{dt} &= \dot{m}^* \left(Y_i^\circ - Y_i^*\right) + \omega_i^* \qquad \left[\frac{\text{kg of } i}{\text{kg fine structure} \cdot \text{s}}\right],
\end{aligned} \tag{4.27}$$

where p is the pressure, h is the enthalpy, and Y_i is the mass fraction of species i. Superscripts * and $^\circ$ refer to fine structure and surrounding fluid, respectively.

$-Q^*_{\text{rad}}$ and ω_i^* are the source terms for radiative loss and mass production due to chemical reaction, respectively. The fine structure reactors are assumed to be stationary and the source terms in the reactor equations may now be expressed as.

$$\omega_i^* = \dot{m}^* \left(Y_i^* - Y_i^\circ\right) \tag{4.28}$$

$$Q^*_{\text{rad}} = \dot{m}^* \left(h^* - h^\circ\right) \tag{4.29}$$

By applying Eq. 4.26 and remembering that EDC only allows chemical reactions in the fine structures, the mass averaged chemical production term would be $\widetilde{\omega}_i = \gamma^* \chi \omega_i^*$. However, to take into account that the fine structures exchange mass with the fine structure-regions, the mass averaged term is multiplied by $1/\gamma_\lambda$ [64] leading to

$$\widetilde{\omega}_i = \frac{\gamma^* \chi}{\gamma_\lambda} \omega_i^* \tag{4.30}$$

$$= \gamma_\lambda^2 \chi \dot{m}^* \left(Y_i^* - Y_i^\circ\right). \tag{4.31}$$

4.4.3 Treatment of Chemical Kinetics

The further evaluation of Eq. 4.31 is dependent on the treatment of chemical kinetics. The EDC is capable of handling chemical reactions with a varying degree of complexity, ranging from the fast chemistry limit to a detailed description of the different elementary reactions involved in the combustion process.

Fast Chemistry Limit

The fast chemistry limit is obtained by assuming that the combustion can be represented by a single one-step infinitely fast irreversible reaction

$$1 \text{ kg fuel(F)} + r_{\text{F}} \text{ kg oxidant (O)} \longrightarrow (1 + r_{\text{F}}) \text{ kg product (P)} \tag{4.32}$$

where r_{F} is the stoichiometric amount of oxidiser.

χ is the reacting fraction of the fine structures and is modelled as [34, 64]

$$\chi = \chi_1 \cdot \chi_2 \cdot \chi_3 \tag{4.33}$$

where χ_1 is the probability of coexistence of the reactants

$$\chi_1 = \frac{\left(\tilde{Y}_{\min} + \tilde{Y}_P/(1+r_F)\right)^2}{\left(\tilde{Y}_F + \tilde{Y}_P/(1+r_F)\right)\left(\tilde{Y}_O/r_F + \tilde{Y}_P/(1+r_F)\right)}, \tag{4.34}$$

χ_2 expresses the degree of heating

$$\chi_2 = \min\left[\frac{\tilde{Y}_P/(1+r_F)}{\gamma_\lambda\left(\tilde{Y}_P/(1+r_F) + \tilde{Y}_{\min}\right)}, 1\right], \tag{4.35}$$

and χ_3 limits the reaction due to lack of reactants

$$\chi_3 = \min\left[\frac{\gamma_\lambda\left(\tilde{Y}_P/(1+r_F) + \tilde{Y}_{\min}\right)}{\tilde{Y}_{\min}}, 1\right] \tag{4.36}$$

with

$$\tilde{Y}_{\min} = \min\left[\tilde{Y}_F, \frac{\tilde{Y}_O}{r_F}\right] \tag{4.37}$$

By inserting the expressions for χ and applying Eq. 4.26 the mass averaged reaction rate of fuel can be expressed (Eq. 4.31) as [34]

$$\widetilde{\omega}_F = -\frac{\gamma_\lambda^2 \chi_1 \dot{m}^*}{1 - \gamma^* \chi} \min\left[\tilde{Y}_{\min}, \tilde{Y}_P/(1+r_F), \left(\tilde{Y}_{\min} + \tilde{Y}_P/(1+r_F)\right)\gamma_\lambda\right] \tag{4.38}$$

Finite-Rate Chemistry

Finite-rate chemistry is taken into account by solving the coupled differential reactor equations presented in Eq. 4.28. In EDC the fine structure reactors are assumed to be stationary, and the state of the fine structure is found by integrating

Eq. 4.28 from $t = t_0$ to $t = t_0 + \Delta t$, with the limit $\Delta t \to \infty$. This corresponds to a perfectly stirred reactor with residence time $\tau^* = 1/\dot{m}^*$. The fine structure reaction rate of species i (ω_i^*) is found by using a chemical reaction mechanism as described in Sec. 3.4. In the present work the detailed reaction mechanism GRI-Mech. 2.11 [7] is used. GRI-Mech. 2.11 includes 49 species and 279 elementary reactions.

When the state of the fine structures has been determined, the mean chemical production rate can be computed from Eq. 4.31. From the previous discussion of the parameter χ, it seems that χ is a factor that actually takes finite-rate chemistry into account. Gran [34] argues that the detailed reaction mechanism will determine weather reaction will occur or not. Consequently, he propose that χ=1 should be used when finite-rate chemistry is being used. The mass averaged reaction rate of species i is now found from the expression

$$\widetilde{\omega}_i = \gamma_\lambda^2 \dot{m}^* \left(Y_i^* - Y_i^\circ \right). \tag{4.39}$$

4.4.4 Radiation

When radiation is not taken into account the source term Q_{rad}^* in Eq. 4.28 is zero and the fine-structure reactor is adiabatic. In this case the specific enthalpy of the fine structures equals the specific enthalpy of the surroundings. In general, the temperature of the fine structures will differ from the surrounding temperature due to different composition. Due to this variation in temperature and composition, the radiation from the fine structures and surroundings will be unequal. By using Eqs. 4.29 and 4.26, the source term in the mean enthalpy equation (Eq. 4.7) may be expressed as

$$\widetilde{Q} = \gamma^* \chi \dot{m}^* \left(h^* - h^\circ \right) + (1 - \gamma^* \chi) Q_{\text{rad}}^\circ \tag{4.40}$$

where -Q° is the radiative loss from the surroundings. The specific enthalpy of the fine structures is found from integrating Eq. 4.28 until steady state is reached. Both Q_{rad}^* and Q_{rad}° are computed by using the radiation model described in Sec. 3.5. Note that if the flame is not assumed to be optical thin, the implementation of a radiation model in EDC will be a more complex task.

4.4.5 Soot models in EDC

Original EDC soot model

In the original EDC soot model by Magnussen [64, 66], soot is allowed to be formed both in the fine structures and the surroundings, while soot oxidation is taking place solely in the fine structures. The reason for this departure from the treatment of gas-phase reactions, which are restricted to the fine structures, is that soot kinetics are slower than most of the gas-phase reactions.

The amount of nucleus and soot in the fine structures is found in a similar way as the fine structure gas-phase composition. The fine structures are treated as homogeneous reactors

$$\frac{dY^*_{\mathrm{n/s}}}{dt} = \dot{m}^* \left(Y^\circ_{\mathrm{n/s}} - Y^*_{\mathrm{n/s}}\right) + \omega^*_{\mathrm{n/s}} \tag{4.41}$$

where

$$\omega^*_{\mathrm{n/s}} = \omega^*_{\mathrm{n/s,f}} + \omega^*_{\mathrm{n/s,c}} \tag{4.42}$$

The formation terms $\omega^*_{\mathrm{n/s,f}}$ are given by Eqs. 2.16 and 2.19 or Eqs. 2.24 and 2.25 depending on which version of the model that is used. The combustion terms $\omega^*_{\mathrm{n/s,c}}$ are given by Eq. 2.21. The reactor is assumed to be homogeneous and the fine structure state is found by integrating Eq. 4.41 until steady state is achieved.

The mean reaction rates for soot and nucleus can be found by mass averaging the reaction rates in the fine structures and surroundings, see Eq. 4.26

$$\widetilde{\omega}_{\mathrm{n/s}} = \gamma^* \chi \omega^*_{\mathrm{n/s,f}} + \left(1 - \gamma^* \chi\right) \omega^\circ_{\mathrm{n/s,f}} + \gamma^* \chi \omega^*_{\mathrm{n/s,c}} \tag{4.43}$$

Note that nucleus and soot is formed both in the fine structures and surroundings, while combustion of soot only occurs in the fine structures.

By assuming steady state for the fine structure reactor and using Eq. 4.41, the mean reaction rates for formation of nucleus and soot may be written

$$\widetilde{\omega}_{\mathrm{n/s}} = \gamma^* \chi \dot{m}^* \left(Y^*_{\mathrm{n/s}} - Y^\circ_{\mathrm{n/s}}\right) + \left(1 - \gamma^* \chi\right) \omega^\circ_{\mathrm{n/s,f}} \tag{4.44}$$

Soot models by Moss and Lindstedt

In the present predictions, all chemical reactions in soot formation and oxidation are restricted to the fine structures. The reason for this change of strategy from the original EDC soot model, is that it is desirable to treat the soot chemistry in the same way as the rest of combustion chemistry. The objective of the present work is to include different soot models into the EDC, not to develop EDC-specific models. It is desirable to establish a framework which allows importing any soot model developed for laminar flames, into the EDC in the same way as ordinary chemical reaction schemes for combustion are imported. This strategy is supported by recent results where the EDC has been used to predict other slow chemical processes such as NO_x formation [58]. In this work, the elementary reactions governing NO_x formation and consumption were included in the same manner as the other gas-phase reactions. Computed mass fractions of NO were compared to experimental data and the agreement was generally good.

The mean source terms in the mass averaged equations for soot particle number density and soot mass fraction is now expressed as

$$\widetilde{\omega}_{\mathrm{N}} = \gamma_{\lambda}^{2}\dot{m}^{*}\left(Y_{\mathrm{N}}^{*} - Y_{\mathrm{N}}^{\circ}\right) \tag{4.45}$$

$$\widetilde{\omega}_{\mathrm{s}} = \gamma_{\lambda}^{2}\dot{m}^{*}\left(Y_{\mathrm{s}}^{*} - Y_{\mathrm{s}}^{\circ}\right) \tag{4.46}$$

The mass fraction and particle number density of soot in the fine structures are found in a similar way as the gas-phase composition. Equations for Y_{N}^{*} and Y_{s}^{*} equivalent to Eq. 4.28 are integrated from $t = t_0$ to $t = t_0 + \Delta t$, with the limit $\Delta t \rightarrow \infty$. The fine structure net production rates ω_{N}^{*} and ω_{s}^{*} are computed according to Eqs. 2.29 and 2.30 in Sec. 2.2.2. Due to the need for intermediate species, this soot model can only be applied when using a detailed representation of the gas-phase chemistry.

Two-way coupling of gas-phase and soot kinetics

The formation and oxidation of soot particles will lead to a transfer of mass between the gas-phase species and the soot particles. In earlier work, this interaction

between the soot and gas-phase chemistry, has usually not been included in numerical models for turbulent combustion. There are several reasons for making this simplification. In many cases, the soot yield is so low that the consumption and formation of gas-phase species due to formation and oxidation of soot particles is negligible. However, since formation and oxidation of soot is dependent on minor intermediate species, it seems likely that soot reactions might influence the concentration of these species, and thereby alter the flame structure. This effect may be noticeable even at relatively low concentrations of soot.

Another reason for ignoring the interaction between soot and gas-phase is that it in many cases is difficult to model. When using an assumed pdf-flamelet combustion model, the gas-phase state is normally found from a flamelet library and is then used as input in the soot model. This approach makes it difficult to take the two-way coupling between soot and gas-phase chemistry into account. The EDC however, has the flexibility to account for this two-way coupling.

In the present work a simplified approach for including the two-way coupling of soot and gas-phase chemistry has been used. Soot is treated as a gas-phase species, but with some simplifications. Soot is not included in the calculations of enthalpy and average properties such as R, c_p, and μ. It is not clear how the soot particles will influence these average properties, but knowledge of the thermodynamic and transport properties of soot particles would be required. General expressions for these properties for soot are not known. However, it is assumed that this simplification is justified as long as $Y_\mathrm{s} \ll 1$. The most physically correct strategy would probably be to treat the flame as a reacting two-phase flow where soot is modelled as particles. This would add a high degree of complexity to the modelling, and to keep the code useful for simulations of practical interest, a simplified approach has been chosen.

The source terms in the mass conservation equations for the species which participates in the soot model are adjusted according to the soot model equations

$$\frac{dY^*_{i,\mathrm{s}}}{dt} = \dot{m}^* \left(Y^\circ_{i,\mathrm{s}} - Y^*_{i,\mathrm{s}}\right) - \dot{\omega}^*_{i,\mathrm{s}} + \dot{\omega}^*_i = 0, \tag{4.47}$$

where $\dot{\omega}^*_i$ is the reaction rate of species i given by the chemical reaction mechanism (e.g. GRI-Mech. 2.11), and $\dot{\omega}^*_{i,\mathrm{s}}$ is the consumption rate of species i due

to soot kinetics. This consumption rate will be positive for C_2H_2, O_2, and OH because these species are consumed due to soot formation and oxidation. The consumption rate for the species H_2, H, and CO will be negative because these species are products in the chemical model-reactions for soot formation and oxidation (cf. Eqs. 2.31, 2.34, 2.40, and 2.41).

Chapter 5

Numerical Method

All simulations presented in this report are performed with the general-purpose CFD code SPIDER. SPIDER uses curvilinear non-orthogonal coordinates and can be used to simulate both non-reacting and reacting turbulent flows. The computer code was developed by Melaaen [68, 70, 69] and has been further extended by Gran [34, 35, 36] to include various combustion models. The various numerical techniques and algorithms used in the present work is thoroughly discussed in these references. Only a brief description of the numerical methods, used in the present work, is given in the following sections.

The Graphical User Interface LIZARD [96] has been used for grid-generation and setup of initial- and boundary-conditions prior to the simulations.

5.1 Discretisation

The model transport equations can be expressed in the form of the mean scalar transport equation (cf. Eq. 4.8)

$$\frac{\partial}{\partial t}\left(\bar{\rho}\tilde{\phi}_i\right) + \frac{\partial}{\partial x_j}\left(\bar{\rho}\tilde{\phi}_i\tilde{v}_j\right) = \frac{\partial}{\partial x_j}\left(\Gamma_{\text{eff},i}\frac{\partial\tilde{\phi}_i}{\partial x_j}\right) + \overline{S}_i, \tag{5.1}$$

where $\Gamma_{\text{eff},i}$ is the effective diffusivity. The finite-volume method is applied and the equation is integrated over a general control volume, δV_P, in physical space. By using the Gauss divergence theorem, and applying implicit Euler discretisation in time, the following equations appear

$$a_P\varphi_P = \sum_{\text{nb}} a_{\text{nb}}\varphi_{\text{nb}} + b \tag{5.2}$$

where

$$a_P = \sum_{\text{nb}} a_{\text{nb}} + a_P^\circ + a_{\text{f}} - \overline{S}_{2P} \tag{5.3}$$

$$b = b_{\text{NO}} + a_P^\circ\varphi_P^\circ + \overline{S}_{1P} \tag{5.4}$$

$$a_P^\circ = \frac{\rho_P^\circ\,\delta V_P}{\Delta t} \tag{5.5}$$

and

$$a_{\text{f}} = \frac{\rho_P - \rho_P^\circ}{\Delta t}\delta V_P + F_e - F_w + F_n - F_s + F_t - F_b. \tag{5.6}$$

In these equations, subscript $_{\text{nb}}$ refer to the neighbouring nodes surrounding the central node P. The subscripts $_e$, $_w$, $_n$, $_s$, $_t$, and $_b$ refer to the control volume faces, east, west, north, south, top and bottom. Superscript $^\circ$ means values from previous time step and Δt is the time step interval. The non-orthogonal terms b_{NO} are not described here, but can be found in [34].

The terms F_{nn} in Eq. 5.6 represent the mass flow across the various control volume faces

$$F_{nn} = (\rho \hat{U}^i)_{nn} \tag{5.7}$$

where $\hat{U}^i$ is the volumetric flow rate in the i direction at surface nn.

The source term S has been linearised according to

$$\overline{S}_P = \int_{\delta V} S dV = \overline{S}_{1P} + \overline{S}_{2P}\, \varphi_P \tag{5.8}$$

where $\overline{S}_{1P}$ gives the constant part of the source and $\overline{S}_{2P}$ is the coefficient of the variable part. To avoid a numerically unstable solution, $\overline{S}_{2P}$ must be negative.

The convective terms are discretisised with the second-order upwind scheme (SOU). This scheme is of second-order accuracy, but can in some cases lead to numerical un-stabilities. In cases where this was a problem, the power-law scheme (POW) was used to obtain a converged calculation. These results where then used as initial conditions for the final calculations with the SOU scheme. The POW scheme is more robust than the SOU scheme, but can give false diffusion at high Peclet numbers (the ratio of the strengths of convection and diffusion) [77]. The convective terms are approximated using central differences. More details on the schemes used in SPIDER is given by Melaaen [68] and Gran [34].

5.2 Solution Algorithm

In SPIDER a collocated grid is used and the Cartesian velocity components are stored in scalar grid-points. To estimate the convective flux at a control volume face, the velocity at the face is needed. This velocity is found by the Rhie & Chow interpolation method [83] which has good convergence and stability properties.

The SIMPLE algorithm [77] is chosen to find updated velocity and pressure fields obeying the discrete momentum and continuity equations for the converged solution. First, tentative velocity and pressure fields are guessed. These fields are corrected by solving a pressure-correction equation derived from the continuity

equation [68, 77]. The deduced pressure-correction equation has the same form as Eq. 5.2. The solution algorithm is as follows:

1. Guess initial conditions for all variables.
2. Update the boundary conditions.
3. Solve the momentum equations.
4. Find the mass flow by the Rhie and Chow interpolation formula.
5. Solve the pressure-correction equation.
6. Correct the pressure, mass flow rate and Cartesian velocity components.
7. Solve the k and ε equations.
8. Solve the enthalpy equation, the mean mass fraction equations, and the soot equations.
9. Calculate the temperature, density and viscosity.
10. Use the new values as initial conditions, and repeat Steps 2 to 9 until convergence is reached.

The set of algebraic equations that results from the discretisation are solved sequentially with line-by-line TDMA together with block-correction. The solution is regarded as converged when the 1-norm of the residuals scaled against a representative inflow flux is small (typically 10^{-4}) for all variables.

5.2.1 EDC Model in Spider

The eddy dissipation concept (EDC) is used to express the source terms in the transport equations for mean enthalpy, mean mass fractions, mean soot particle number density, and mean soot volume fraction. The EDC model is discussed in Sec. 4.4. Here, the numerical implementation of EDC in the CFD program SPIDER is described. The EDC model enters in Steps 9 in the solution algorithm presented above.

Step 9:

9 a. Compute the fine-structure state based on fast- or detailed chemistry (see below). If fast chemistry is assumed, the one-step, irreversible, and infinitely fast reaction in Eq. 4.32 is used to compute the fine structure composition.

When a detailed description of chemical kinetics is used, the fine structure gas-phase composition and enthalpy is found by integrating the homogeneous reactor equations, Eq. 4.28, until steady state is reached. The chemical reaction rates, ω_i^*, are found from Eqs. 3.32 and 3.33. The calculation is performed by using subroutines from the chemical program library CHEMKIN II [49]. The radiative source term, Q_{rad}^*, is found from Eq. 3.42 The integration of the reactor equations are performed with the program package LIMEX [18].

9 b. If soot is included in the calculations, compute soot particle number density of the fine-structures, Y_{N}^*, and the fine structure soot mass fraction, Y_{s}^*. This is done in a similar way as for the gas-phase composition with finite rate chemistry. Homogeneous reactor equations for Y_{N}^* and Y_{s}^* are integrated until steady state is achieved. For this integration the ode-solver LSODE [42] is used. The source terms, ω_{N}^* and ω_{s}^* are found from Eqs. 2.30 and 2.29.

9 c. Compute the composition and enthalpy of the surrounding fluid from Eq. 4.26.

9 d. Compute the temperature in the surrounding fluid from Eq. 3.3 by Newton iteration.

9 e. Compute the surrounding fluid density from the equation of state, Eq. 3.1.

9 f. Compute the surrounding fluid viscosity from Eq. 3.7.

9 g. Determine the mean temperature, density and viscosity from the fine-structure and surrounding states by using Eq. 4.26 or its volume-averaged counterpart.

Chapter 6

Turbulent Jet Diffusion Flame of Methane and Air

In this section results from simulations of a turbulent jet diffusion flame of methane are presented. The flame is studied experimentally by Brookes and Moss [10, 12]. Results from the simulations are compared with experimental data for temperature, mixture fraction, and soot volume fraction.

6.1 Experimental Setup

The burner is described in detail by Brookes et al. [10, 12] and only a short description is given here. The burner is of a confined piloted circular type. The cylindrical nozzle consist of a 4.07 mm diameter orifice for the main fuel flow. To stabilise the flame, this orifice is surrounded by an annular premixed pilot of 160 μm width. The nozzle and flame are contained by a Pyrex tube of diameter 155 mm. The Pyrex tube is split into two sections separated by a slotted stainless steel ring to allow optical and probe access to the flame. The Pyrex tube may be traversed horizontally to allow measurements at different positions. Operating

conditions for the flame investigated are given in Table 6.1. The pilot flame is a fuel-rich mixture of methane and oxygen with a methane flow rate less than 2% of the main fuel flow rate.

Table 6.1: Operating conditions for the investigated flame.

Absolute pressure	1 atm.
Fuel mass flow	10.3 g/min
Air mass flow	708 g/min
Fuel temperature	290 K
Air temperature	290 K
Fuel jet velocity	20.3 m/s
Exit Reynolds number	5000

6.2 Previous Predictions

To test and verify models for soot formation in turbulent combustion it is necessary to compare predicted results with reliable experimental data. It is necessary to compare not only soot volume fractions, but also other characteristic data as temperature and mixture fraction. Unfortunately, it is difficult to make reliable measurements of all these variables in a sooting flame because the appearance of soot tends to complicate measurements. As a result, few such cases are reported in the literature. The experimental data by Brookes and Moss provides a splendid possibility to test coupled models for turbulent combustion, soot and radiation. Consequently, several authors have used this flame as a test case for their mathematical models. A short review of previously published results from numerical simulations of this particular flame is given below.

6.2.1 Brookes and Moss

Brookes and Moss who studied this case experimentally, also performed numerical predictions of the flame [13]. They used a modified version of the GENMIX computer code, which is a 2D parabolic CFD-program. The models used includes the k-ε turbulence model with a round-jet correction and a laminar flamelet combustion model with a presumed Beta function PDF. For modelling soot formation and oxidation the model by Moss was used. This is the same model which is presented in Sec. 2.2.2.

The authors used two different strategies for incorporating the soot model into the presumed Beta function combustion model. The first strategy is to assume that the soot properties are totally uncorrelated with the mixture fraction and each other. This assumption yields only limited success. The predicted amount of soot in the flame is close to the experimental values only when soot oxidation is omitted in the model. When soot oxidation is included, the peak soot volume fraction is under-predicted by more than two orders of magnitude.

The other strategy is to assume that soot properties are perfectly correlated with the mixture fraction. This is difficult because one needs to know the joint PDF of the soot variables and the mixture fraction, and this is generally not known. The authors solve this by introducing a normalised profile of soot mass concentration from an appropriate laminar flame calculation. It is assumed that the profiles will have the same shape, but different magnitude, in the turbulent case. This profile is then imposed on to the mean soot properties in the turbulent case. This approach leads to some numerical difficulties [9] and the authors have to introduce a minimum threshold value in the normalised profile of soot mass concentration. The value of this threshold influences the result of the calculation. Because the correct threshold value cannot be found prior to the calculations the generality of the model is questionable.

6.2.2 Kronenburg, Bilger and Kent

Kronenburg and co-workers [53] used the conditional moment closure (CMC) method to model the turbulent combustion. The turbulence model used was a k-ε model where some of the model constants were modified to get a good representation of the spreading of the jet. The model constant $C_{\varepsilon 1}$ (cf. Eq. 4.14) was allowed to vary according to

$$C_{\varepsilon 1} = 1.4 - 3.4 \left(\frac{\tilde{k}}{\tilde{\varepsilon}} \frac{\partial \tilde{u}}{\partial x} \right)_{\mathrm{c}}^{3} \tag{6.1}$$

where subscript c refers to the centerline value. This expression was first proposed by Morse [72] and has also been used by Liew et al. [57]. $C_{\varepsilon 2}$ was given the value 1.85.

Soot formation and oxidation were modelled by the Lindstedt version of the model presented in Sec. 2.2.2 and the effects of differential diffusion of the soot particles were investigated. It was found that by setting the molecular diffusion coefficient of the soot variables equal to zero, good agreement between predicted and measured soot volume fractions along the centerline was obtained. When assuming equal diffusion coefficients for all species and soot variables the centerline soot volume fractions were under-predicted by 17%. The authors argue that molecular diffusion of the soot particles tend to zero in comparison with the molecular diffusion of the gaseous species. The effect of zero diffusivity of soot particles has also been studied by Kollmann et al. [52]. Kollmann and co-workers predicted soot volume fractions in a turbulent ethylene jet-flame using an empirical soot model. The expressions for soot formation and growth were functions of temperature and mixture fraction. These correlations were derived from measurements in a laminar diffusion flame. Unlike Kronenburger and co-workers, Kollmann found that predicted soot volume fractions decreased when zero diffusivity for soot was assumed.

6.2.3 Roditcheva and Bai

In her Ph.D. work, Olga Roditcheva [84] performed a numerical study of both the 1 atm. flame and the 3 atm. flame experimentally studied by Brookes and Moss. Part of the work is also published elsewhere [85]. She used the same approach for combustion modelling as Brookes and Moss by using a laminar flamelet model with a presumed PDF. To model the soot chemistry she used an earlier version of the Moss model [73, 92] than the one presented in Sec. 2.2.2. Good agreement with measured values of soot volume fractions was obtained by adjusting some of the model parameters.

6.3 Present Predictions

Since the burner is axisymmetric a two-dimensional version of the Spider code has been used. The flame is assumed to be axisymmetric and the computational domain in the transverse direction is defined by the centerline and the radius of the surrounding Pyrex tube. This is the same approach used in the works described in the previous section.

6.3.1 Computational Grid

Several different grids has been used simulating this flame. It was found that to avoid a grid-dependent solution a relatively fine grid had to be used. In all the presented calculations a grid with 80 lines in the stream-wise direction and 70 lines in the transverse direction has been used. The grid is nonuniform and rectilinear. The lines in the transverse direction are chosen to coincide with the burner centerline, the radius of the fuel jet, the radius of the pilot jet, and the radius of the surrounding Pyrex tube.

6.3.2 Boundary and Inlet Conditions

Brookes and Moss do not report information about the inlet profiles used in the experiments. In the present work, plug profiles have been used for velocity, turbulent kinetic energy, and dissipation of turbulent kinetic energy at both the fuel stream and the co-flowing air. Simulations with several different profiles have been performed and it has been found that the development of the jet is quite insensitive to the choice of inlet profiles.

For the axial velocities the mass average values have been used, 20.3 m/s for the fuel jet and 0.55 m/s for the air stream. The required inlet values for the different inlets are given in Table. 6.2

Table 6.2: Inlet values for turbulent methane flame

	Fuel	Pilot	Air
u (m/s)	20.3	5.0	0.55
k (m^2/s^2)	1.54	0.05	0.05
ε (m^2/s^3)	500	0.03	0.03
T (K)	290	290	290

6.3.3 Prediction of flow field and temperature

Predicted and measured values of temperature and mixture fraction along the centerline and at different axial positions are shown in Fig. 6.1. Both the solid and dotted lines represent results from the simulations. The differences between these lines are related to different soot models and will be discussed in the next section. In this section the results represented by the solid line are discussed.

Looking at the results along the centerline (6.1a) it is clear that the spread of the jet is underpredicted. The computed mixture fraction falls too slowly along the centerline because the mathematical model predicts a too slow mixing of fuel and air. This effect is also seen in the computed temperature profile which increases

too slowly. This effect seems to be strongest close to the nozzle and weaker further downstream where the agreement between computed and measured mixture fractions and temperatures is much better.

The inaccurate prediction of the mixing of the jet is also recognised in the radial profiles. Close to the centerline the computed mixture fractions are too high and they fall too quickly towards the edge of the flame.

In previous predictions of this flame various modifications have been applied to obtain an acceptable representation of the spread of the jet. Brookes et al. [13] and Kronenburg et al. [53] have used different round-jet modifications in the k-ε model, while Roditcheva [84] has used the standard model.

The prediction of turbulent mixing and turbulent transport is, of course, mainly governed by the turbulence model. As mentioned earlier, a k-ε model has been used in the present work. This model is widely used for both scientific and engineering purposes. The model is also quite simple and generally gives reasonable results. However, a known weakness of the model is its handling of round jets, where it is known to overpredict the spread of the jet [87]. The aim of this work is not to study turbulence modelling in general, but to study how soot chemistry is affected by turbulence. To make it easier to isolate effects by the soot chemistry it is desirable to use a turbulence model which predicts the turbulent transport in the flame with sufficient accuracy. Several strategies for optimising the standard k-ε model have therefore been tested in the present work. The following adjustments in the k-ε model has been tested for the present case.

- A round-jet correction of the model constant $C_{\varepsilon 2}$ (cf. Eq. 4.14). The value of the constant was changed from 1.92 to 1.83. By reducing $C_{\varepsilon 2}$ the dissipation of turbulence kinetic energy will increase and the spread of the jet will be reduced. $C_{\varepsilon 2} \approx 1.8$ has been found to give a good representation of a non-reacting free flow jet [20]. However, this correction was not sufficient for the present case.
- The turbulent Prandtl and Schmidt numbers were reduced from the standard value of 0.7 to 0.5. This lead to a much better agreement between the measured and predicted spread of the jet close to the nozzle. However, the

results further downstream in the areas where soot formation and oxidation is taking place, were not improved.

- A round-jet correction proposed by Pope [80]. This correction is described in Sec. 4.3 (cf. Eq. 4.17). This correction method gave the best overall representation of the flame. And all results presented in this work have been computed with this correction method. However, as is evident from the presented results, even with this correction model there are notable differences between the measured and predicted values for mixture fraction. A further discussion of these differences is given below.

Unfortunately, the turbulence model is not the only part of the mathematical modelling which may lead to an inaccurate prediction of the turbulent transport. As mentioned earlier, the inlet values for turbulence energy (k) and dissipation of turbulence energy (ε) in the experiment are not known. Using values different from the experimental values will lead to uncertainties in the prediction of the turbulent transport and mixing close to the nozzle. Further downstream, however, the jet is quite insensitive to the inlet values of k and ε.

Other sources of uncertainties in the prediction of turbulent mixing are difficulties related to modelling the burner. Brookes and Moss report that they used the maximum Reynolds number which gave a stable flame attached to the nozzle rim. Consequently, the flame was very close to lift-off or extinction. This caused difficulties for the physical models used in the present work. The EDC has proven to be able to accurately predict lift-off in turbulent diffusion flames [14, 75]. However, a correct prediction of lift-off requires a correct prediction of the turbulent mixing. The EDC predicts lift-off or extinction when the residence time for the fine structure reactor τ^* (cf. Sec. 4.4.3) is less than the necessary residence time for the chemical reactions to occur. The fine structure residence time is directly dependent on $\tilde{k}$ and $\tilde{\varepsilon}$ and inaccuracy in these variables will lead to an erroneous τ^*. As discussed earlier, the prediction of turbulent mixing close to the burner is uncertain and this is probably the main reason for predicting a too low τ^*. Because the flame is close to lift off, even small errors in the predicted residence times may shift the flame from being attached to the burner, to being lifted. To avoid the prediction of lift-off, τ^* was multiplied by a factor of 100 at the grid

points in the vicinity of the burner. The region where τ^* was modified extends ca 4 cm downstream the nozzle and ca 0.5 cm in the radial direction. This adjustment resulted in an stable and attached flame. The modification is not expected to affect other parameters of the simulated flow.

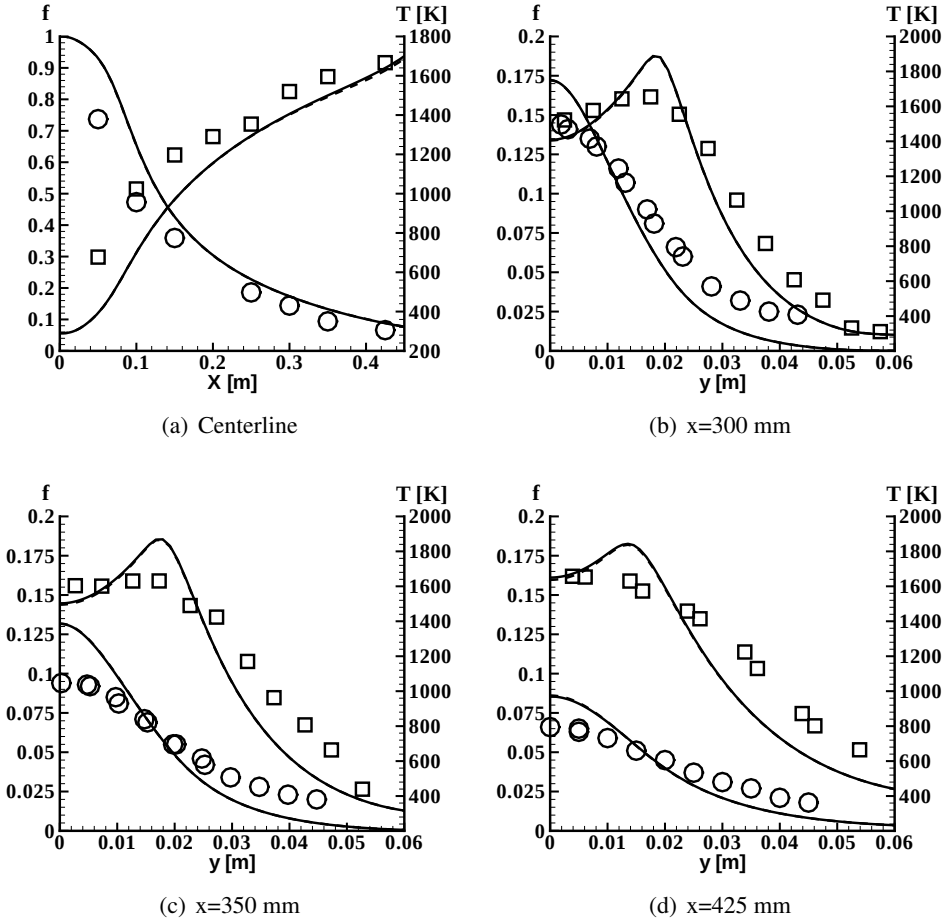

(a) Centerline (b) x=300 mm

(c) x=350 mm (d) x=425 mm

Figure 6.1: Temperature and mixture fraction at centerline and at three different axial positions. Fine grid, Pope correction, Solid line with two-way coupling, dashed without. Moss version of soot model.

6.3.4 Soot predictions

In this section, results from simulations both with and without a two-way coupling of the gas-phase and soot kinetics are presented and discussed. The main emphasis is put on how this two-way coupling influences the predicted soot loads, However, the two-way coupling also effects the temperatures and the flow field. These effects are also discussed below. All results presented in this section is performed with the Moss version of the soot model. Predicted soot volume fractions and experimental values at the centerline are shown in Fig. 6.2a. together with experimental values. The solid line represents the simulations with the two-way coupling and the dashed line the simulations without two-way coupling. The onset of soot formation is found at the same axial position in both simulations and corresponds well with the measured values. Both models overpredict the maximum soot volume fractions at the centerline, but the model with the two-way coupling is closer to the experimental values than the model without the two-way coupling. The measured peak soot volume fraction at the centerline is 1.62×10^{-7} and the value predicted with the two-way coupling is 20% higher. Without the two-way coupling the centerline peak value is overpredicted by 50%.

Predicted and measured values of soot volume fractions at three different axial positions are presented in Fig. 6.2 b – d. At all three positions the model with a two-way coupling predicts lower soot volume fractions than the model without the two-way coupling. Close to the centerline both models overpredicts the soot levels, but with the model with a two-way coupling beeing closest to the experimental values. Further away from the centerline the discrepancies between the measured and predicted soot volume fractions increase. In the radial plot at x=300 mm both soot models predict a peak in the soot volume fractions located off the centerline. This peak is not seen in the experimental values.

At all positions the radial profiles of predicted soot volume fractions fall too quickly towards the edge of the flame, and the deviation increases downstream from from the nozzle. The experimental results show a sooting zone which is growing in the radial direction when travelling downstream. The simulations predicts a sooting zone which has a nearly constant extent in the radial direction.

These discrepancies between the predictions and measurements are at least partly due to the inaccurate prediction of the turbulent transport of the jet. However, the discrepancy between the computed and measured soot volume fractions are larger than for the computed mixture fractions. The most important reasons for the too narrow soot zone in the simulations are probably unaccuracies related to the soot growth and soot oxidation rates. To investigate this more closely predicted rates of nucleation, growth, and oxidation of soot are shown in Fig. 6.3. In the same figure, predicted mole fractions of C_2H_2 and OH are also shown together with an indication of the location of the stoichiometric mixture fraction. The Figs. 6.3a – c corresponds to Figs. 6.2b – d, but notice that the range of the two x-axes are not the same. At all three axial positions acetylen is found on the rich side of the flame and the concentration falls steeply before reaching the stoichiometric position. Due to the linear dependence of acetylene on soot mass growth in the model, the soot mass growth rate also decreases rapidly before reaching the stoichiometric position. In this rich part of the flame soot oxidation is negligable due to a negligable presence of oxidizing species. These results indicate that the prediction of a too narrow sooting zone is related to the soot growth rate and not to the soot oxidation rate.

The prediction of a too narrow sooting zone may also be related to the diffusion of soot particles. In the present work the diffusivity of the soot particles is set equal to the diffusivity of all the other species. This strategy may be questioned because the soot particels are much heavier than the gas-phase particles and therefore should be more resistant to diffusion. Other researchers have made findings supporting a lower diffusivity of the soot particles [52, 53]. However, results from introductory computations with the present models and zero diffusvity of soot particles (not shown), indicate no improvements over the presented results

When discussing the predicted radial profiles of soot volume fractions it should also be noted that Brookes reports that the measurements at the outer part of the flame are more uncertain than close to the centerline [53]. This is due to the post-processing of the measurements. Brookes and Moss measured extinction profiles which were converted into soot volume fractions by use of polynomial curve fitting. Due to the low soot concentrations and a high signal-to-noise ratio only a low-order polynomial fit could be used. The actual shape of the measured

soot volume fractions in the radial direction is therefore uncertain, even though the magnitude of the error is within the limit of 50 %

The two-way coupling of soot and gas-phase chemistry also influences the flow field and temperature of the flame. The flame chemistry is of course altered due to the added reactions. The two-way coupling introduces an extra sink term for the species acetylene, OH, and O_2. At the same time, the soot chemistry includes source terms for the species H_2, H, and CO. The different gas phase composition and different soot volume fractions will lead to different radiation properties of the flame. Volume fractions of the species H_2, C_2H_2 and OH at the centerline predicted both with and without two-way coupling are shown in Fig. 6.4. As expected the two-way coupling results in a lower concentrations of acetylen and OH while the concentration of H_2 is increased. The changes in concentration introduced by the two-way coupling are however small. The changes in CO, H, and O_2 volume fractions due to two-way coupling where not noticeable in the figure and are not shown.

The most important cause of changes in radiation properties is the lower soot yield which gives a lower radiative loss from the flame. The effect of two-way coupling on the computed temperatures and mixture fractions is shown in Fig. 6.1 where the solid lines represent results from calculations with two-way coupling and dashed lines without two-way coupling. In all of the figures, the differences are hardly noticeable. Only in the areas with the highest soot yield a slight difference is noticeable. From Fig. 6.1a it is seen that the two-way coupling leads to a slightly higher temperature far downstream the nozzle, where the soot volume fraction is at its peak value. From the same figure it is clear that the effect on computed mixture fractions are negligable. The same trends are seen in the plots of the radial profiles (Figs. 6.1b-c). Slightly higher temperatures computed with the two-way coupling in areas with high soot yield and minimal effect on the computed mixture fractions.

The calculated peak temperatures off the centerline are not affected by the two-way coupling.

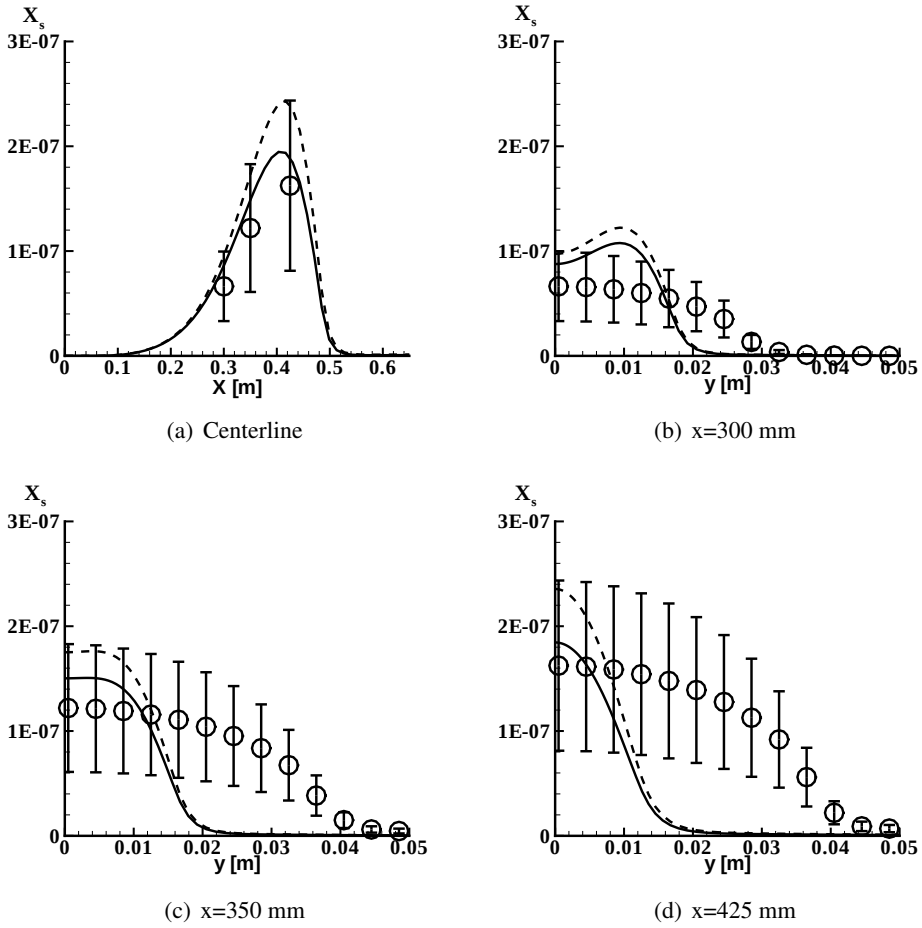

(a) Centerline (b) x=300 mm

(c) x=350 mm (d) x=425 mm

Figure 6.2: Soot volume fractions at centerline and at three different axial positions. Fine grid, Pope correction, Solid line with two-way coupling, dashed without. Mossversion of soot model.

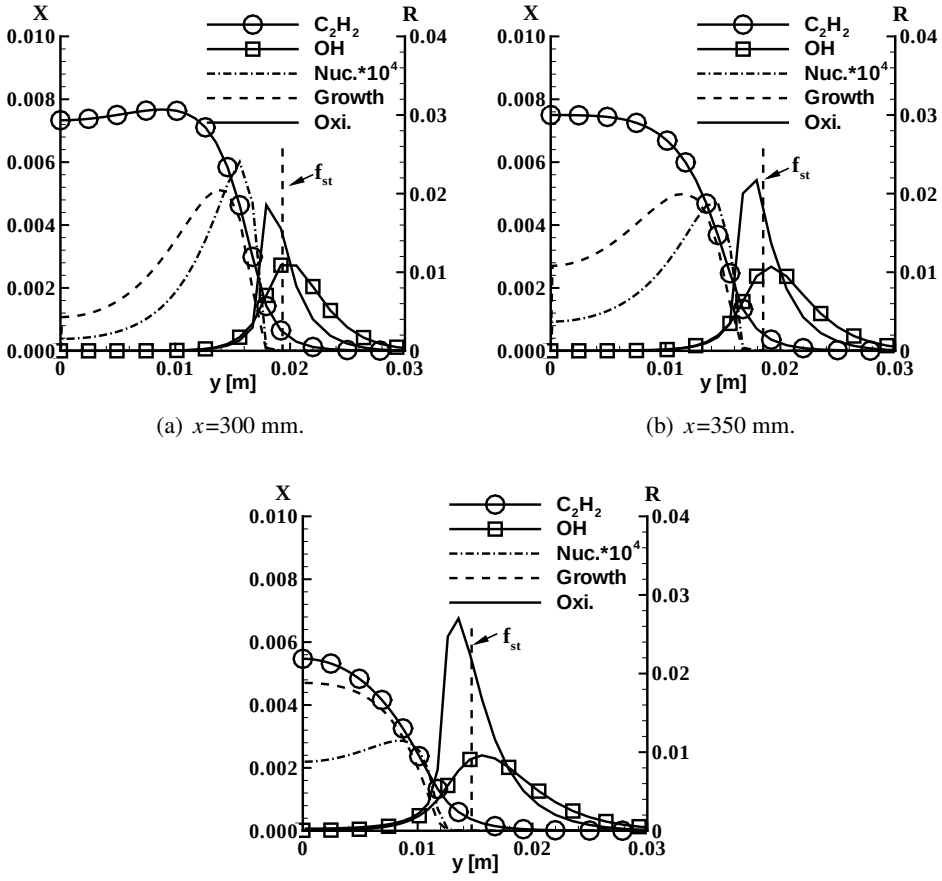

(a) x=300 mm.

(b) x=350 mm.

(c) x=425 mm.

Figure 6.3: Predicted mole fractions of C_2H_2 and OH together with source terms in the soot mass fraction equation. The source terms are represented by the right y-axis and have unit (kg soot)/(m^3). The vertical dotted line indicates the location of the stoichiometric mixture fraction.

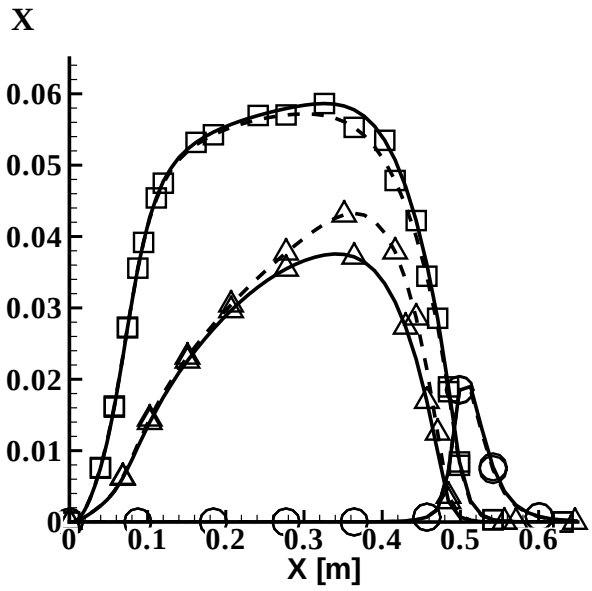

Figure 6.4: Predicted volume fractions of species in the soot model. Square: H_2, Delta: C_2H_2 × 5, Circle: OH × 10. Solid line: with two-way coupling, Dashed line: without two-way coupling. Moss version of the soot model

6.3.5 Effect of soot model

In this section results from simulations with both the Lindstedt version and the Moss version of the soot model are presented and discussed. All results presented in this subsection has been computed with two-way coupling of the soot kinetics and the gas phase kinetics. Profiles of soot volume fractions along the centerline and radial profiles at three different axial positions are shown in Fig 6.5.

Looking at the computed results along the centerline it is seen that the soot volume fractions computed with the Moss model are very close to the measured values. The soot volume fractions are slightly overpredicted, but well within the error limit of 50 %. The Lindstedt model predicts a higher soot yield than the Moss model. The peak soot volume fraction at the centerline found with the Lindstedt model is approximately 1.5 times higher than with the Moss model. The onset of soot formation at the centerline is found approximately at the same axial position with both models, but the build up of soot is faster for the Lindstedt model. The Lindstedt model reaches its peak soot volume fraction slightly upstream of the Moss model.

The overpredicted soot volume fractions at the centerline is also seen in the radial profiles (Fig. 6.5b-d). From the radial profiles it is seen that both models predicts a too narrow soot zone. Both models behaves similarly and the soot volume fractions falls too quickly towards the edge of the flame. This effect is discussed in the previous section. In the radial plot at x=300 mm both soot models predict peak soot volume fractions located off the centerline. This is not seen in the experimental values.

At all axial positions the Moss version of the soot model predicts a lower soot yield than the Lindstedt version. Examining Tab. 2.2 this is not surprising. The pre-exponential factors in the Arrhenius rate expressions for both nucleation (A_1) and mass growth (A_2) are higher in the model by Lindstedt. A_1 is approximately 20 times higher, and A_2 is approximately 1.5 times higher in the Lindstedt model compared to the model by Moss. It is the mass growth which is responsible for the major contribution to the soot volume fraction and it is different A_2 parameters that is the main reason for the discrepancies between the computed profiles.

The effects of soot model on temperature and mixture fraction are hardly noticeable (not shown), but with a slightly higher temperature for the Moss model due to a lower radiative loss from soot.

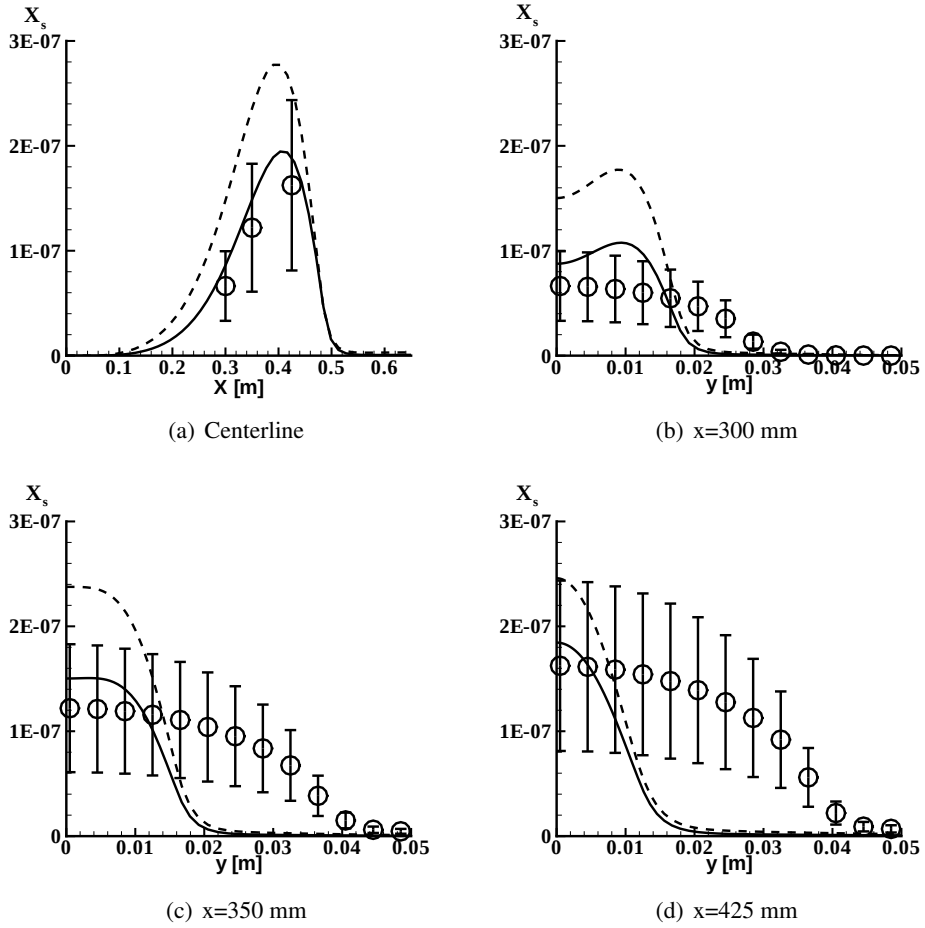

(a) Centerline (b) x=300 mm

(c) x=350 mm (d) x=425 mm

Figure 6.5: Soot volume fractions at centerline and at three different axial positions. Fine grid, Pope correction, and two-way coupling. Solid line Moss model, dashed Lindstedt model.

6.3.6 Effect of Radiation

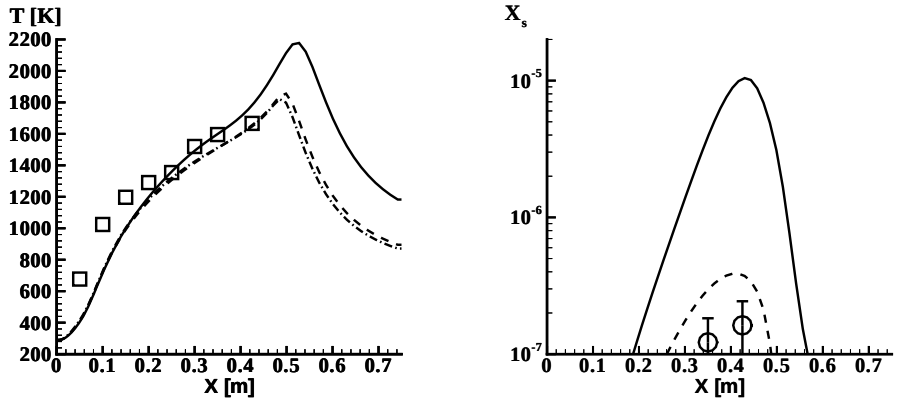

(a) Temperatures at centerline. Solid line: no radiation, dashed: radiation from gas-phase species only, dash-dot: full radiation model.

(b) Soot volume fractions at centerline. Lindstedt soot model, no two-way coupling. Solid line: no radiation, dashed: full radiation model.

Figure 6.6: Effect of radiation on centerline temperatures and soot volume fractions.

There is a strong coupling between soot and radiation in a flame. Soot has a high emissivity and high soot levels in a flame will lead to a substantial radiative transfer of thermal energy from the flame. This heat loss will of course lower the temperature of the flame. At the same time the formation of soot is very temperature dependent. It is therefore very important to account for the radiative heat loss in an accurate way.

To show the importance of of radiative heat transfer in this flame results from simulations both with and without radiation are shown in Fig. 6.6. Fig. 6.6a shows predicted centerline temperatures for three different cases, with no radiation model, with radiation from gas-phase species only, and with radiation from gas-phase species and soot. It is evident that radiation has a major influence on the flame. The maximum predicted temperature at the centerline decreases from 2175 K in the adiabatic case to 1815 K in the case with a full radiation model.

Simulations with radiation from gas-phase species only predicts a maximum centerline temperature of 1859 K. From these results, gas-phase radiation seems to be dominant in the present flame because adding radiation from soot lowers the maximum temperature with only 44 K. However, it is important to remember that the radiative loss is not a linear function of temperature. If predictions were carried out with radiation from soot only, the maximum centerline temperature would still drop considerable below the adiabatic value. Predictions with radiation from soot only has not been performed.

Predicted soot volume fractions at the centerline with and without radiation are shown in Fig. 6.6b. The difference is tremendous. Without radiation the predicted maximum soot volume fraction is 25 times higher than with the full radiation model. This illustrates how sensitive the soot model is to temperature.

6.3.7 Summary

- Results from simulations of a sooting turbulent jet flame is presented and compared with experimental data reported in the literature.
- Predictions are carried out with two similar soot models. Both models have been used with and without two-way coupling of soot kinetics and gas phase kinetics.
- The standard k-ε turbulence model overpredicts the spread of the jet. By using a round-jet correction in the k-ε model the predicted spread of the jet is improved and the computed mixture fractions are in reasonable agreement with the experimental values. There are, however, still noticeable differences between the computed and measured mixture fractions.
- Both soot models overpredicts the soot yield close to the centerline, but by introducing two-way coupling of soot and gas-phase kinetics the results are improved.
- The soot model by Moss predicts lower soot volume fractions close to the centerline than the model by Lindstedt, and the centerline values are very

close to to the experimental values. Both models predicts a too narrow sooting zone. This is partly due to the erroneous spread of the jet, but the measurements are also more uncertain away from the centerline.

- Taking into account the uncertainties of the rather simple soot and radiation models as well as those of the experiments, the agreement of the predicted and experimental data is considered satisfactory.

Chapter 7

Turbulent Jet Diffusion Flame of Ethylene and Air

For a further test of the models, a turbulent jet of ethylene has been studied. This flame is sooting more heavily than the methane-jet presented in the previous chapter. Due to the relatively high soot levels, the influence of soot chemistry on the gas-phase chemistry will be more important. A higher soot yield will also lead to a higher radiative loss from the flame. The ethylene flame is therefore more of a challenge for the coupling of soot, gas-phase kinetics and radiation.

7.1 Experimental Setup

The jet has been experimentally studied by Kent and Honnery [51]. The burner consists of a cylindrical nozzle with a diameter of 3 mm. The burner is aligned vertically and the fuel is burned in still air. Operating conditions for the flame are given in Table 7.1.

Table 7.1: Operating conditions for the ethylene flame.

Absolute pressure	1 atm.
Fuel temperature	322 K
Air temperature	290 K
Fuel jet velocity	52 m/s
Exit Reynolds number	15,100

7.2 Previous Predictions

This flame has also been subject to numerical investigation by several authors. Brief summaries of their findings are given below.

7.2.1 Kent and Honnery

In addition to investigating the flame experimentally, Kent and Honnery [51] modelled soot as a unique function of mixture fraction. This function was deduced from the experimental results. The computed soot volume fractions were qualitatively in agreement with the measured values, but it was found that soot could not be modelled as a unique function of a single scalar.

7.2.2 Said, Garo, and Borghi

Said et al. [88] used a soot model based on a single step global reaction to model soot formation in the turbulent ethylene flame by Kent and Honnery. The formation and oxidation of soot was dependent on mass fractions of fuel, oxidiser, soot, and an intermediate species as well as temperature and pressure. Necessary reaction rate parameters were found experimentally from measurements in a laminar diffusion flame of Ethylene and air. This model was then incorporated in the PEUL (probabilistic Eulerian Lagrangian) turbulent combustion model. Good agreement between numerical and measured values of soot volume fractions in

the turbulent flame were obtained. However, a shortcoming of the model is that it has to be modified to be used with other fuels than ethylene.

7.2.3 Pitsch, Riesmeier, and Peters

Pitsch and co-workers [79] reported results from a numerical study with detailed chemistry of the ethylene flame by Kent and Honnery. A k-ε model and a presumed pdf for the mixture fraction was used together with the unsteady flamelet model to simulate the flame. The unsteady flamelet model was used with a chemical reaction scheme which included aromatic compounds up to pyrene. In addition, further growth of polycyclic aromatic hydrocarbons was accounted for by the HACA mechanism. Soot inception, growth and oxidation were calculated by flamelet equations for the two first statistical moments of the soot particle size distribution. These two equations corresponds to mean particle number density and total soot mass. This chemical reaction scheme and soot model have earlier been used to predict soot in a laminar flame by Mauss et al. [67]. Very good agreement between predicted and experimental values of soot volume fractions were obtained. Pitsch et al. also studied the influence of differential diffusion in the flamelets on soot particles. Calculations were performed both with unity Lewis numbers for all particles and with diffusion coefficients dependent on the soot particle size. The authors found that the results including differential diffusion seemed to be in closer agreement with the experimental results. However, the results did not provide a basis for recommending one of the methods.

7.3 Present Predictions

As in the methane case, the flame is assumed to be axisymmetric and the same two-dimensional version of the Spider code has been employed for the ethylene flame. Unlike the methane flame, the ethylene flame is not bounded by a wall as the fuel jet expands into still air. This causes some numerical difficulties for Spider which is an elliptic code. To obtain a stable numerical solution for the flame, it

is necessary to use a solid wall as the boundary condition in the axial direction at the outer radius of the computational domain. The computational domain has to be made large enough to minimise the effect of this wall on the flame. In addition, the air at the boundary in the radial direction, outside the jet, must have a small velocity in the axial direction. Consequently, the simulations have been performed with a weak co-flow of air. The axial velocity of the co-flowing air was set as low as possible, still providing a stable solution to the simulations. A velocity of 0.5 m/s was found to be the minimum value possible to use. Compared to the jet velocity of 52 m/s it is likely that the effect of this weak co-flow of air has a negligible effect on the flame. The computational domain expands 1.1 m downstream the nozzle, in the axial direction, and 0.12 m in the radial direction. This corresponds to 367 and 40 nozzle diameters respectively. To check that the effect of the outer wall on the predictions are negligible, Predictions has also been performed with a grid which expands 0.24 m in the radial direction. Radial profiles of predicted temperatures with both grids are shown in Figure 7.1. These test predictions have been performed with the fast chemistry assumption.

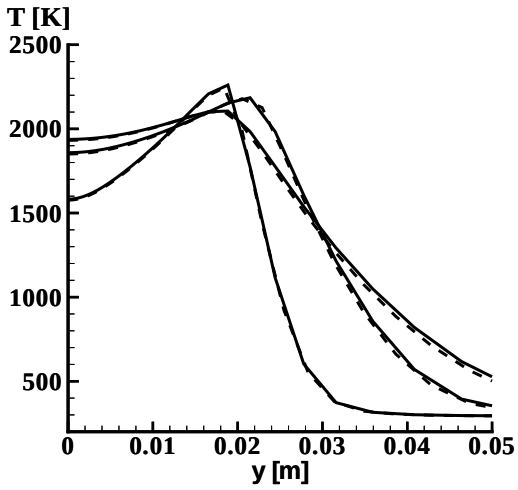

Figure 7.1: Radial profiles of predicted temperature at three axial positions. Solid line: wall at 0.12 m, dashed line: wall at 0.24m. Fast chemistry assumption.

7.3.1 Computational Mesh

The grid used in the simulations presented below consist of 41 lines in the axial direction and 38 lines in the radial direction. The grid i nonuniform and rectilinear with the closest grid-spacing close to the nozzle where the gradients are high. The grid is shown in Figure 7.2. To make sure the solution is not dependent of the grid, simulation have also been performed on a 76 $\times$ 82 grid. Predicted temperatures and mixture fractions at the centerline from simulations with both grids are shown in Figure 7.3. These predictions have been performed with the fast chemistry assumption. The discrepancies between the two simulations are seen to be small and it is assumed that the less dense grid is sufficiently accurate.

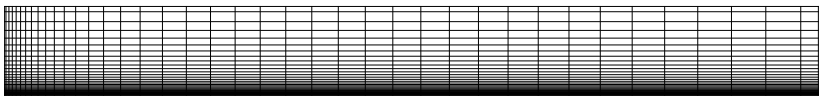

(a) 41 $\times$ 38 grid

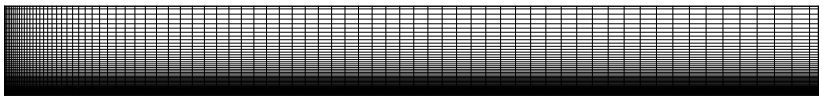

(b) 76 $\times$ 82 grid

Figure 7.2: The two different grids used in the simulations.

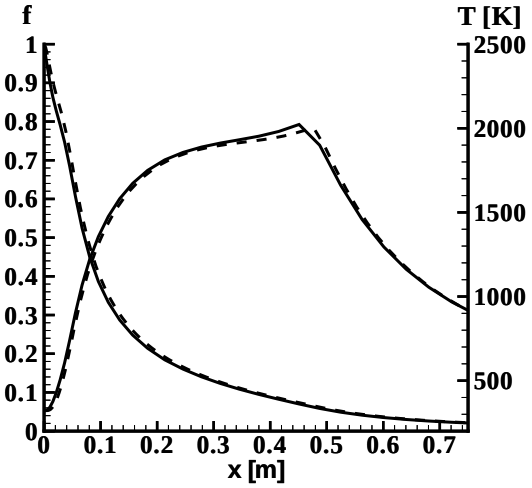

Figure 7.3: Predicted mixture fractions and temperatures at centerline. Solid line: 41 × 38 grid, dashed line: 76 × 82 grid.

7.3.2 Inlet Conditions

The only inlet conditions reported by Kent and Honnery are the temperature and the mass average velocity of the jet. In the numerical simulations plug profiles have been used for velocity, turbulent kinetic energy and dissipation of turbulent kinetic energy. The inlet values for the fuel jet, used in the present simulations are given in Table 7.2 The values of k and ε given in Table 7.2 corresponds to

Table 7.2: Inlet values for the turbulent ethylene jet flame

u (m/s)	52.0
k (m^2/s^2)	15
ε (m^2/s^3)	10,000
T (K)	322,15

a turbulence intensity of 6 % and a turbulent integral length scale equal to the

nozzle diameter. To study the effect of these parameters on the flow-field, several simulations were performed with different inlet values for k and ε. Predicted radial profiles of temperature at three different axial positions are shown in Figure 7.4. Three different sets of inlet values have been used. The solid line shows the results with the values given in Table 7.2. The dashed line is predicted with lower turbulence intensity on the inlet. Here the turbulence intensity is reduced to 0.5 % and the integral turbulent length scale is set to 3 % of the nozzle diameter. The dash-dotted line is predicted with a turbulence intensity of 12 % and a length scale twice the nozzle diameter. The fast chemistry assumption has been used for all three cases. Even though these predictions have been performed with fast chemistry, Figure 7.4 provides useful information of how the flow field is affected by the inlet parameters. In particular, it is interesting to observe how the spread of the jet is influenced. It was found that the change in the spread of the jet was negligible when the detailed chemistry was used instead of the fast chemistry assumption. It is therefore assumed that the effects of inlet parameters on the spread of the jet, seen in Figure 7.4, would be similar if detailed chemistry had been used. As expected, low turbulence level results in a broad flame, while high turbulence results in a faster spread of the jet. It was found that the inlet values represented by the solid line and given in Table 7.2 gave the best representation of the spread of the jet compared to the experimental data. These inlet values are used in all results presented later in this chapter. Comparison with experimental data and a further discussion of the predicted flow field is given in the next section.

7.3.3 Prediction of Flow Field and Temperature

Predicted and experimental profiles of temperature and mixture fractions at the centerline are shown in Fig. 7.5a. The solid lines are results from the simulations with a two-way coupling. The dashed lines are results from simulations without a two-way coupling. As in the Methane case, the k-ε turbulence model has been used with the round-jet correction of Pope. All simulations have been performed with the Moss soot model. The mixture fraction at the centerline is well predicted and the effect of the two-way coupling on the mixture fraction is small. The effect on the predicted temperatures is much more distinct. Close to the nozzle it

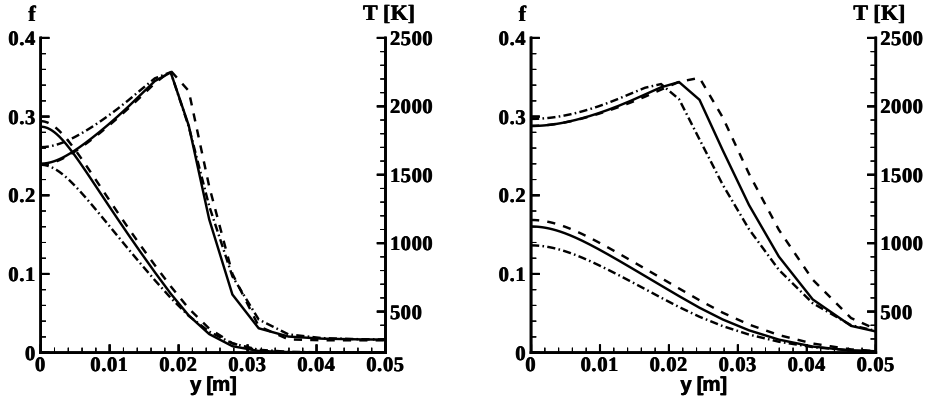

(a) x=13.8 cm.

(b) x=24.2 cm.

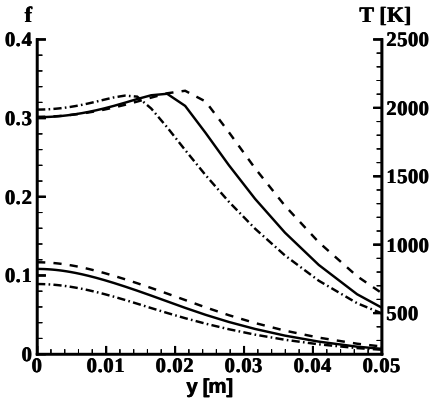

(c) x=34.5 cm

Figure 7.4: Temperature and mixture fraction at three different axial positions with three different sets of turbulent inlet values at the fuel jet. Solid line: moderate turbulence, dashed line: low turbulence, dash-dotted line: high turbulence.

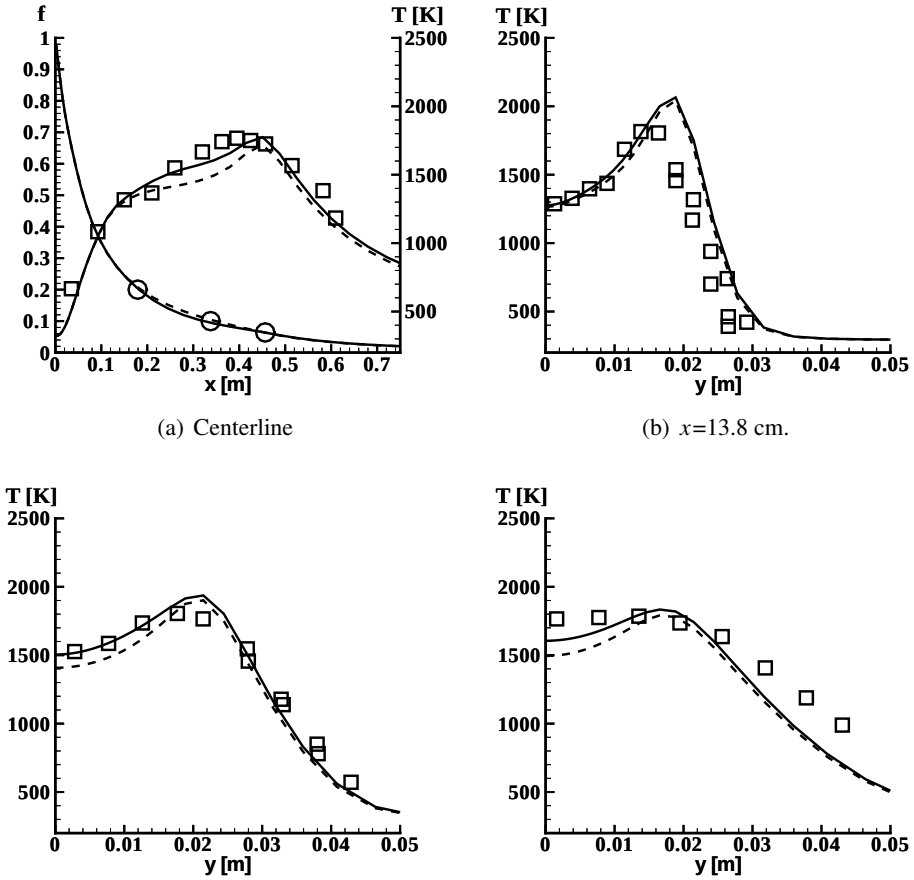

(a) Centerline

(b) x=13.8 cm.

(c) x=24.2 cm

(d) x=34.5 cm.

Figure 7.5: Temperature at the centerline and three different axial positions. At the centerline the mixture fraction is also shown. Solid line is computed with two-way coupling. Dashed line without two-way coupling. The Moss soot model is used in both simulations.

is difficult to separate the different simulations, but approximately 15 cm downstream the two versions start to differ. The simulations with the two-way coupling predict a higher temperature than the standard model. The maximum difference between the predicted temperatures is approximately 200 K and the simulations with the two-way coupling are in much closer agreement with the experimental result than the standard version. As will be discussed later, the region with the largest difference between the predicted temperatures coincides with the region with the highest soot yield.

Radial profiles of computed and measured temperatures are shown in Figures 7.5b–c. The predicted temperatures are generally in good agreement with the measured values, but three are some important discrepancies. At the position closest to the nozzle, the temperature peak is overpredicted. The location of the peak temperature is also shifted outwards in the flame compared to the experimental values. At this axial location the spread of the jet seems to be slightly overpredicted. Unfortunately, no radial profiles of measured mixture fractions have been reported. At the axial position 24.2 cm downstream the nozzle the temperatures are well predicted throughout the flame. Further downstream, at x=34.4 cm, the predicted temperature profile deviates somewhat from the experimental results. Close to the centerline the temperature is underpredicted, whilst at the outer part of the flame, the predicted temperatures decay too rapidly.

7.3.4 Soot Predictions

In this section the effects of using a two-way coupling of soot and gas-phase kinetics are studied. Radial profiles of predicted an experimental soot volume fractions at 4 different axial positions are shown in Figures 7.6a-d. The solid lines represents predictions with a two-way coupling, and the dotted lines represent predictions without a two-way coupling of soot and gas-phase chemistry. At the axial positions 13.8 cm and 24.2 cm the soot volume fractions are severely overpredicted. The centerline soot volume fractions predicted with the two-way coupling are 4.3 and 3.5 times higher than the experimental values at these two positions. At the position closest to the nozzle the predicted soot volume fractions reach a

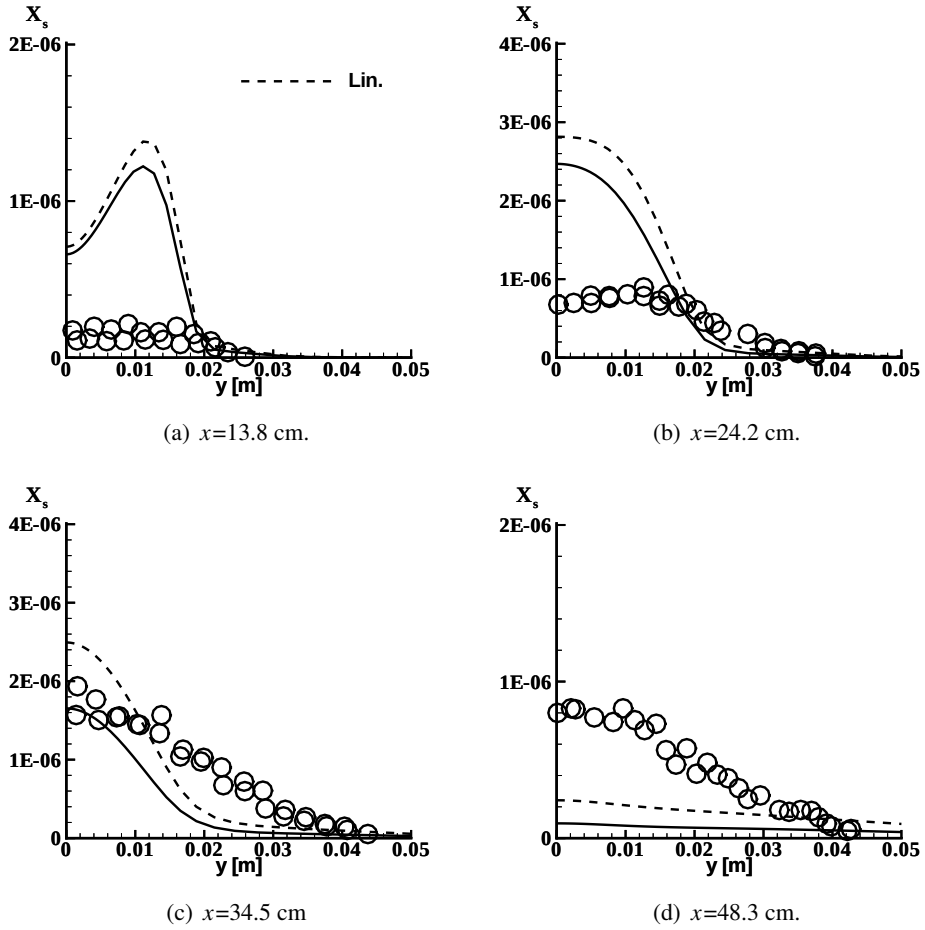

(a) x=13.8 cm. (b) x=24.2 cm.

(c) x=34.5 cm (d) x=48.3 cm.

Figure 7.6: Computed and experimental soot volume fractions at three different axial positions. Solid line is computed with two-way coupling. Dashed line without. Moss soot model is used in both simulations.

peak located off the centerline. The experimental results do not exhibit such a peak value. One reason for this erroneous shape of the predicted soot volume fractions may be found by examining the temperature profile at the same axial position, Figure 7.5b. The maximum temperature is overpredicted by almost 500 K. The discrepancies between measured and predicted temperatures are mainly found outside the sooting region at this location. Nevertheless, badly predicted temperatures earlier in the flame may also influence soot at this location. Further tests to investigate the effect of overpredicted temperatures on soot formation are presented and discussed later in this section.

At the axial position 34.5 cm downstream the nozzle the predicted profiles which maps the measured values best, is found. The soot model with the two-way coupling predicts the correct soot volume fraction at the centerline, but the predicted soot volume fractions fall too quickly towards the edge of the flame. Comparing with the temperature profiles at the same axial position, Figure 7.5d, it is seen that this trend is also found in the predicted temperatures. One cause of this too fast decay of soot volume fractions might therefore be inaccurate representation of the spread of the jet. At x=48.3 cm the soot volume fractions are severely underpredicted. From the above discussion, the physical models seem to predict soot too early in the flame. Soot starts to build up too early and reaches a maximum earlier in the flame than the experimental results. At the four axial positions shown in Figure 7.6 the predicted maximum soot volume fraction is found at x=24.2 cm The experimental maximum, however, is found at the position further downstream, at x=34.5. At x=48.3 cm most of the soot is oxidised in the predictions, whilst in the experimental results there is still soot left in the flame.

As expected, predictions with the two-way coupling results in lower and more correct soot volume fractions at all of the axial positions. The largest discrepancies between the two models are found in Figure 7.6c at x=34.5 cm Here the soot volume fraction at the centerline is reduced by from 2.5×10^{-6} to 1.6×10^{-6} (36% reduction) with the two-way coupling. To examine the necessity of the two-way coupling of soot and gas-phase chemistry it is interesting to compare the amounts of carbon in soot and in acetylene which is the species responsible for soot inception and growth in the present model. The predicted maximum concentration of acetylene at the centerline is approximately 5×10^{-4} kmol/m^3 and the maximum

concentration of soot at the centerline corresponds to an acetylene concentration of approximately 1.5×10^{-4}kmol/m^3. This means that a two-way coupling between soot and gas-phase-chemistry is important. In the model, all the carbon in the soot particles originates from acetylene and when the amount of carbon in soot and acetylene is of the same level, it is likely that the interaction of soot and gas-phase chemistry is important for the flame characteristics.

For a better understanding of the behaviour of the soot model it is useful to examine the source terms in the soot mass fraction equation. Radial profiles of these source terms are shown in Figure 7.7. Predicted mean mole fractions of the species which are responsible for soot growth (C_2H_2) and oxidation (OH) are also shown together with an indication of the location of the predicted stoichiometric mixture fraction. The axial positions of Subfigures 7.7b-d corresponds to the Subfigures 7.6a-c showing predicted soot volume fractions. Subfigure 7.7a is included to give information about soot chemistry upstream the first experimental results.

At all axial locations acetylene is found on the rich side of the flame and the concentration falls rapidly close to the stoichiometric position. Soot nucleation and mass growth are linear functions of the acetylene concentration and therefore these terms are also only found in the rich part of the flame. At all the locations the source term due to mass growth is substantially larger than the source term due to nucleation. It is also seen that the peak value for soot mass growth does not coincides with the maximum acetylene concentration. This is especially evident at the two axial positions closest to the nozzle. The reason for this shift is the high activation temperature in the Arrhenius expression for the soot rate constant. At low temperatures the soot mass growth is limited due to this high activation temperature. At all axial positions the peak concentration of OH is found at the point of the stoichiometric mixture fraction. The activation temperature in the Arrhenius expression for the rate constant of oxidation by OH is zero, and the profile of the OH oxidation rate closely follows the OH concentration profile.

The highest soot mass growth rates are found at the axial position 13.8 cm (Figure 7.7b). This is also the location where the discrepancy between the predicted and measured soot volume fractions (Figure 7.6a) is the largest. Comparing these figures more closely it is seen that the erroneous predicted maximum soot volume

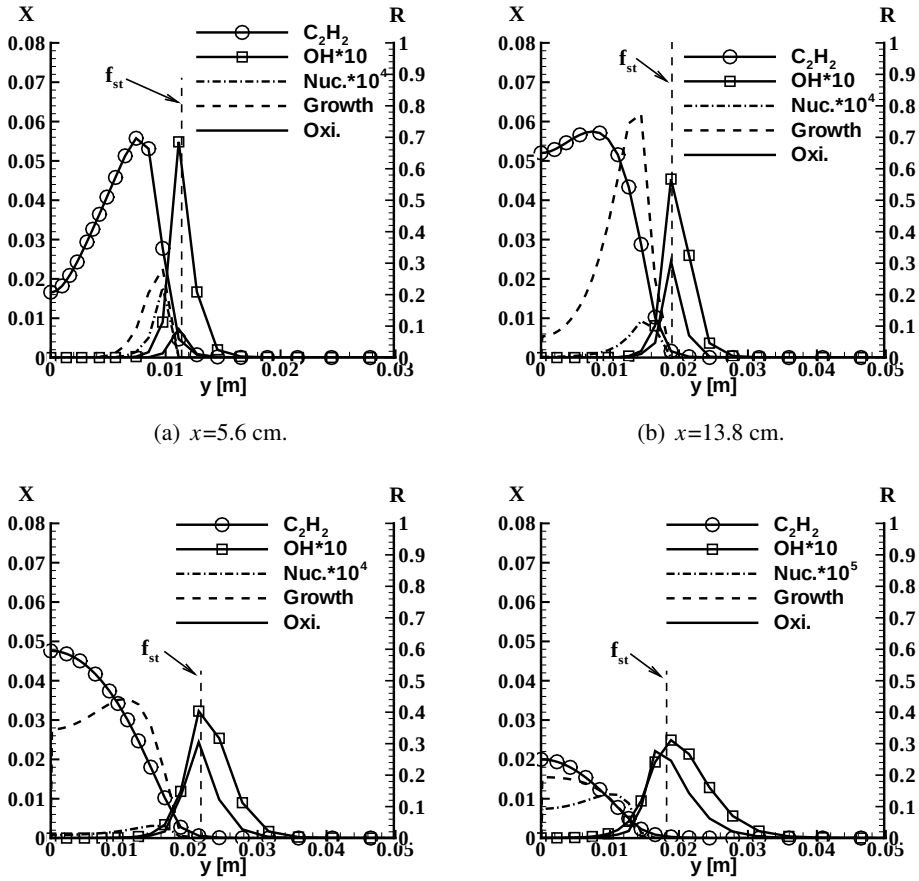

(a) x=5.6 cm. (b) x=13.8 cm.

(c) x=24.2 cm. (d) x=34.5 cm.

Figure 7.7: Predicted mole fractions of C_2H_2 and OH together with source terms in the soot mass fraction equation. The source terms are represented by the right y-axis and have unit (kg soot)/(m^3). The vertical dotted line indicates the location of the stoichiometric mixture fraction.

fraction occurs at the same location as the maximum soot mass growth rate. This finding indicates that the soot level in the vicinity of this peak is due to a too high mass growth rate, and not due to large amounts of soot being convected to this location. Assuming the overpredicted soot yield is due to a too high soot mass growth rate in this area, it is interesting to look at the predicted and measured temperatures at the same axial location. This is shown in Figure 7.5b. As mentioned earlier, the maximum temperature is overpredicted and the peak is shifted outwards in the flame compared to the experimental values. However, the temperature in the rich part of the flame is very well predicted. If the temperature dependence in the expression for the soot mass growth rate is correct, the overpredicted soot mass growth rate may be connected to the predicted acetylene level in several ways. The assumption of soot mass growth based purely on acetylene concentration is crude, and the simple linear dependence of mass growth on concentration may not be appropriate at all conditions. The predicted concentration of acetylene may deviate from the levels in the actual flame. Because there are no measured values of acetylene for the present flame, it is difficult to estimate the correctness of the predicted acetylene concentrations. There are also uncertainties connected to the coupling of soot chemistry and turbulence, that is how well the EDC handles the soot chemistry. With the present results, it is difficult determine the relative importance of these factors.

Even though the temperatures in the soot growth region of the flame at x=13.8 cm are well predicted, inaccuracies in the predicted temperatures upstream this point may lead to erroneous predicted soot levels at this position. To study the effect of temperature on soot prediction a simulation with reduced temperature in the soot model was performed. In this simulation the temperature used in the gas-phase kinetics was unchanged from the simulations presented previously in this section. The radiation loss was also kept unaltered. The only change was that the temperature used in calculating the source terms in the soot model was reduced by 2 %. The reason for changing the temperature in the soot model only, was to isolate the effect of temperature on the soot predictions. The resulting soot volume fractions are shown in Figure 7.8. It is immediately clear that this small reduction in temperature has a major impact on the prediction of soot. At all the axial locations the predicted soot yield is significantly reduced. At x=13.8 cm

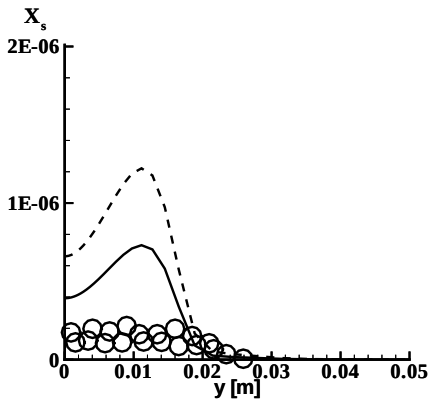

(a) x=13.8 cm.

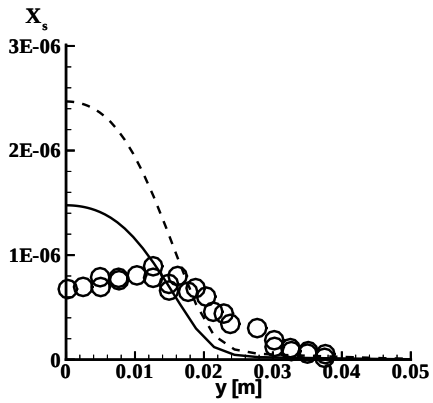

(b) x=24.2 cm.

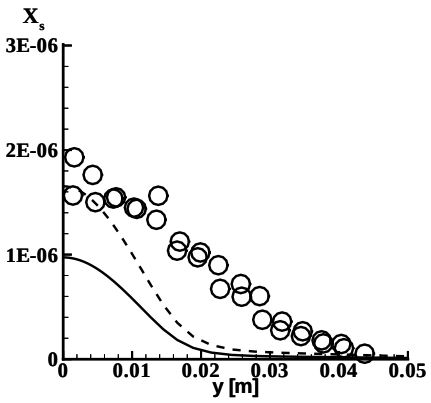

(c) x=34.5 cm.

Figure 7.8: Soot volume fractions with reduced temperature in soot model. Solid line: temperature reduced with 2% in soot model, dashed line: no reduction in temperature.

the maximum soot volume fraction is reduced from 1.22×10^{-6} to 0.78×10^{-6}, a reduction of 36%. The shape and extent of the sooting region is almost unaltered by the reduced temperature. As in the case with no reduction in temperature, these simulations predicts the maximum centerline soot level too early in the flame.

7.3.5 Effect of soot model

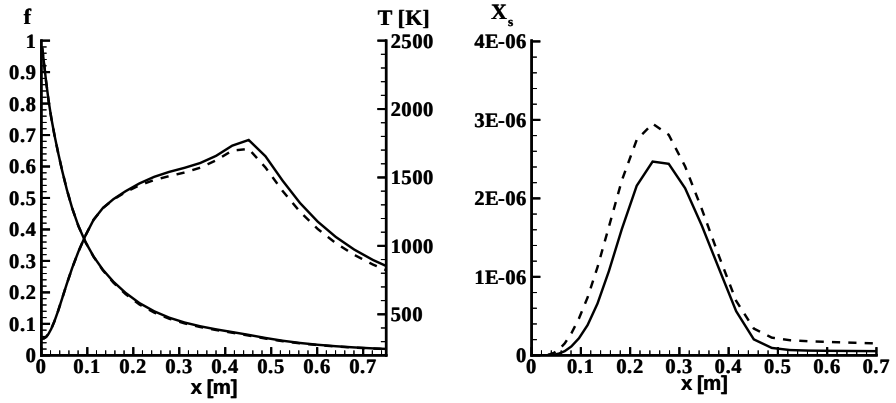

(a) Temperature (b) Soot volume fractions

Figure 7.9: Predicted temperatures and soot volume fractions at centerline. Solid line: Moss soot model, dashed line: Lindstedt soot model. Predictions with two-way coupling of soot and gas-phase.

Predictions of soot in the present Ethylene flame has also been performed using the Lindstedt soot model. Predicted values of mixture fraction, temperature and soot volume fraction are shown with dotted lines in Figure 7.9. For comparison, results obtained with the Moss soot model is also shown, with solid lines. Two-way coupling of soot and gas-phase kinetics has been used in both simulations. The differences between the predictions with the two models show the same trends as in the methane case presented in section 6.3.5. The discussion given for the methane flame also applies to the present flame, and only the most important

differences in the results using the two models, are commented here. Again, the mixture fraction is negligible affected by the choice of soot model. As expected, the temperature computed with the Lindstedt model is slightly lower than with the Moss model. This is due to the higher soot yield predicted with the Lindstedt model. In accordance with the findings in the previous chapter, the Lindstedt soot model predicts higher soot levels than the Moss model. Also for the present case the soot level predicted with the Moss model is in better accordance with the experimental values (not shown).

7.3.6 Effect of Radiation

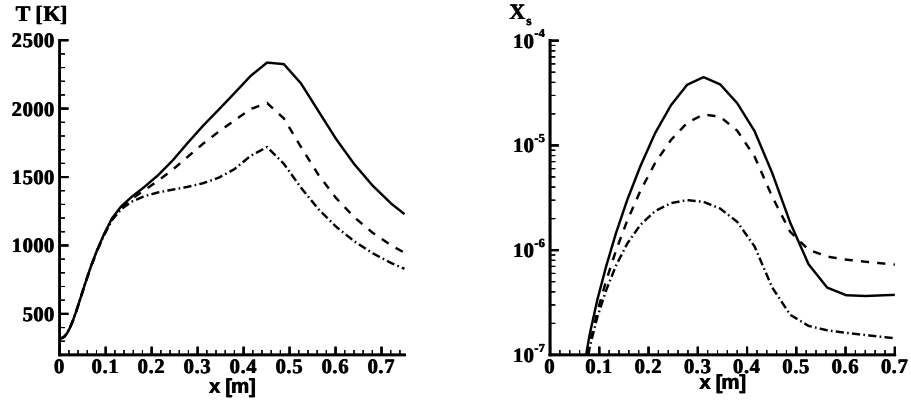

(a) Temperature.

(b) Soot volume fractions.

Figure 7.10: Effect of radiation on centerline temperatures and soot volume fractions. Solid line: no radiation, dashed: radiation from gas-phase species only, dash-dot: full radiation model.

The present ethylene flame has a high soot yield and thereby also a high radiative loss to the surroundings. To illustrate the strong coupling of soot and radiation simulations have been performed with three different levels of radiation included, no radiation, radiation only from gas-phase species, and full radiation

model. Figure 7.10 shows predicted centerline values of temperature and soot volume fractions with the three different levels of radiation included. In this figure all results are obtained without two-way coupling of soot and gas-phase chemistry. The centerline temperature (Figure 7.10a) is the same for all three cases until the sooting region is reached. This region starts approximately 0.12 cm downstream the nozzle and here the mean temperature is close to 1250 K. Further downstream the temperature starts to differ. The maximum difference between the three cases is found at the location where the centerline temperature peaks. The maximum centerline temperature computed without radiation (solid line) is 2310 K, which is close to the adiabatic flame temperature for ethylene (2380 K). The maximum temperature computed with the complete (dash-dotted line) radiation model is 1710 K, 700 K lower than without radiation included. The simulation with radiation only from the gas-phase species (dashed line) peaks at 2015 K. If this figure is compared to the corresponding figure for the methane case, Figure 6.6, it is evident that switching from radiation only from the gas phase to the complete radiation model, has a much stronger effect on the simulation of the ethylene flame. Due to the much higher soot level in the ethylene case, radiation from soot becomes more important.

The predicted soot volume fractions at the centerline, shown in Figure 7.10b, clearly illustrates the importance of temperature on soot formation. Notice the logarithmic y-axis. Again the largest differences are found at the location of maximum soot volume fractions. The maximum centerline soot volume fraction predicted without radiation is 1.35×10^{-5}, whilst with the complete radiation model the maximum value is 1.2×10^{-6}.

7.3.7 Summary

- Results from simulations of a sooting turbulent jet flame of ethylene and air is presented and compared with experimental data reported in the literature. This flame has much higher soot levels than the methane flame presented in the previous chapter.
- The temperature field predicted with the two-way coupling of soot and gas-

phase chemistry is in good agreement with the experimental results.

- The soot model without the two-way coupling underpredicts the maximum temperature at the centerline by 200 K.
- The maximum soot level is overpredicted and the sooting region is shifted upstream compared to the measurements. The soot volume fractions predicted with the two-way coupling is in better agreement with the measurements than the predictions without the two-way coupling.
- In some regions of the flame the predicted amount of carbon in soot and acetylene are of the same level, indicating that the two-way coupling is important for the present flame.
- Results from simulations with different levels of radiation included are presented. These results clearly shows the strong coupling of soot and radiation in the present flame.

Chapter 8

Conclusions and Further Work

8.1 Conclusions

The subject area of the present work has been modelling of soot formation and oxidation in turbulent flames. In particular, the focus has been on the combination of the Eddy Dissipation Concept (EDC) combustion model and various soot models. A major goal has been to study the ability of the EDC to handle soot models developed for laminar conditions.

Two versions of a semi-empirical soot model have been included in the EDC combustion model. The soot equations and kinetics have been included in the EDC in a way similar to the treatment of finite rate gas-phase chemistry. The soot models are included exactly as they were developed, without any tuning of parameters or constants. To model the interaction of soot and gas-phase chemistry, the soot models have been implemented with a two-way coupling of soot and gas-phase kinetics. This means that the amount of a gas-phase specie which is consumed by the soot reactions, is actually removed from the gas-phase composition. Similarly, a gas-phase specie which is a product of the soot reactions, is added to the gas-phase composition.

Sooting flames are often highly radiative, and to account for the radiative loss, a radiation model has been included in the code. The radiation model is based on the assumption of an optical thin flame.

This set of coupled mathematical models have been used to simulate turbulent diffusion flames of methane and ethylene. The results are compared to measurements and the main findings can be summarised as:

- For both the methane and the ethylene jet flame, the spread of the jets was predicted with a certain degree of inaccuracy compared to the experimental values. These difficulties are probably related to uncertain inlet conditions, and that the k-ε turbulence model is not ideally suited for round jet flames.
- The two-way coupling of soot and gas-phase kinetics is found to have a positive effect on the predicted soot volume fractions. Especially, in the ethylene case with the highest soot yield, the two-way coupling improves the results.
- The effect of the two-way coupling on the gas-phase kinetics and flame characteristics is demonstrated. It is found that the influence on the gas-phase concentrations is small, even for the species that are participating in the soot reactions. The two-way coupling seems to have only minor effects on other flame characteristics such as temperature and mixture fraction.
- The importance of the radiation model on the predictions is demonstrated. The assumption of an optical thin flame seems to be sufficient for the flames studied.
- For both flames the, peak soot volume fractions are overpredicted and soot is predicted in a too narrow zone around the centerline. The narrow sooting zone is partly due to the difficulties predicting the correct spread of the jet. In the methane case, the computed soot volume fractions at the centerline are within the uncertainties of the experiments.
- The results are considered to be encouraging. The work has demonstrated that the EDC has the capacity to handle different types of chemical reaction mechanisms, such as mechanisms for gas-phase combustion and soot

kinetics, without modification.

8.2 Further work

- In the flames studied in the present work, there is no knowledge of the gas-phase composition. Consequently, it is difficult to know the correctness of the predicted levels of species participating in the soot reactions such as acetylene, OH, and O_2. Inaccuracies in the amount of these species would, of course, lead to wrong input in the soot models. For a more precise study of how the EDC handles the soot models, flames with measurements of both soot and important gas-phase species should be simulated. However, few such flames are reported in the literature.
- The set of coupled models should be tested on more practical cases, such as gas turbines and chemical reactors.

Bibliography

[1] M. Balthasar, F. Mauss, A. Knobel, and M. Kraft. Modeling of soot formation in a partially stirred plug flow reactor. *Combustion and Flame*, 128:395–409, 2002.

[2] T. R. Barfknecht. Toxicology of soot. *Prog. Energy Combust. Sci.*, 9:199–237, 1983.

[3] R. S. Barlow, A. N. Karpetis, J. H. Frank, and J.-Y. Chen. Scalar profiles and NO formation in laminar opposed-flow partially premixed methane/air flames. *Combustion and Flame*, 127:2102–2118, 2001.

[4] R. B. Bird, W. E. Stewart, and E. N. Lightfoot. *Transport Phenomena*. John Wiley & sons, 1960.

[5] H. Bockhorn, editor. *Soot Formation in Combustion*. Springer-Verlag, 1994.

[6] U. Bonne, K. H. Homann, and H. GG. Wagner. Carbon formation in premixed flames. In *Tenth Symposium (International) on Combustion*, pages 503–512, Pittsburgh, 1965. The Combustion Institute.

[7] C. T. Bowman, R. K. Hanson, D. F. Davidson, W. C. Gardiner, V. Lissianski, G. P. Smith, D. M. Golden, M. Frenklach, and M. Goldenberg. GRImech 2.11. `http://www.me.berkeley.edu/gri_mech/`. Last visited 15 August 2005.

[8] D. Bradley, G. Dixon-Lewis, S. El-Din Habik, and E. M. J. Mushi. In *Twentieth Symposium (International) on Combustion*, page 931, Pittsburgh, 1984. The Combustion Institute.

[9] S. J. Brookes. *Soot Production and Thermal Radiation from Turbulent Jet Diffusion Flames*. PhD thesis, Cranfield University, 1996.

[10] S. J. Brookes. *Soot Production and Thermal Radiation from Turbulent Jet Diffusion Flames*. PhD thesis, Cranfield University, 1996.

[11] S. J. Brookes and J. B. Moss. Measurements of soot production and thermal radiation from confined turbulent jet diffusion flames of methane. *Combustion and Flame*, 116:49–61, 1999.

[12] S. J. Brookes and J. B. Moss. Measurements of soot production and thermal radiation from confined turbulent jet diffusion flames of methane. *Combustion and Flame*, 116:49–61, 1999.

[13] S. J. Brookes and J. B. Moss. Predictions of soot and thermal radiation properties in confined turbulent jet diffusion flames. *Combustion and Flame*, 116:486–503, 1999.

[14] R. Cabra, T. Myhrvold, J. Y. Chen, R. W. Dibble, A. N. Karpetis, and R. S. Barlow. Simultaneous laser raman-rayleigh-lif measurements and numerical modeling results of a lifted turbulent H_2/N_2 jet flame in a vitiated coflow. In *Twenty-Ninth Symposium (International) on Combustion*, Pittsburgh, 2002. The Combustion Institute.

[15] H. F. Calcote and R. J Gill. Comparison of the ionic mechanism of soot formation with a free radical mechanism. In *Soot Formation in Combustion*, pages 471–484. Springer-Verlag, 1994.

[16] A. Coppalle and D. Joyeux. Experimental and theoretical stusies on soot formation in an ethylene jet flame. *Combust. Sci. and Tech.*, 93:375–386, 1993.

[17] P. Coppalle and D. Joyeux. Temperature and soot volume fraction in turbulent diffusion flames: Measurements of mean and fluctuating values. *Combustion and Flame*, 96:275–285, 1994.

[18] P. Deuflhard, E. Hairer, and J. Zugck. One-step and extrapolation methods for differential-algebraic systems. *Numerische Mathematik*, 51:501–516, 1987.

[19] R. B. Edelman and P. T. Harsha. Laminar and turbulent gas dynamics in combustors – current status. *Prog. Energy Combust. Sci.*, 4:1–62, 1978.

[20] I. S. Ertesvåg. *Turbulent Flow and Combustion (Turbulent Strøyming og Forbrenning)*. Tapir Academic Publisher, 2000. In Norwegian.

[21] I. S. Ertesvåg and B. F. Magnussen. The eddy dissipation turbulence energy cascade model. *Combustion Science and Technology*, 159:213–235, 2000.

[22] M. Fairweather, W. P. Jones, R. P. Ledin, and R .P. Lindstedt. Predictions of soot formation in turbulent non-premixed propane flames. In *Twenty-Fourth Symposium (International) on Combustion*, pages 1067–1074, Pittsburgh, 1992. The Combustion Institute.

[23] M. Fairweather, W. P. Jones, and R .P. Lindstedt. Predictions of radiative transfer from a turbulent reacting jet in a cross-wind. *Combustion and Flame*, 89:45–63, 1992.

[24] C. P. Fenimore and G. W. Jones. Comparative yields of soot from premixed hydrocarbon flames. *Combustion and Flame*, 12:196–200, 1968.

[25] A. B. Fialkov. Investigations on ions in flames. *Prog. Energy Combust. Sci.*, 23:399–528, 1997.

[26] M. Frenklach. Reaction mechanism of soot formation in flames. *Phys. Chem. Chem. Phys.*, 4:2028–2037, 2002.

[27] M. Frenklach, D. W. Clary, W. C. Gardiner, Jr., and S. E. Stein. Detailed kinetic modeling of soot formation in shock-tube pyrolysis of acetylene. In *Twentieth Symposium (International) on Combustion*, pages 887–901, Pittsburgh, 1984. The Combustion Institute.

[28] M. Frenklach and H. Wang. Detailed modeling og soot particle nucleation and growth. In *Twenty-Third Symposium (International) on Combustion*, pages 1559–1566. The Combustion Institute, 1990.

[29] M. Frenklach and H. Wang. Detailed mechanism and modeling of soot particle formation. In *Soot Formation in Combustion*, pages 165–192. Springer-Verlag, 1994.

[30] M. Frenklach and J. Warnatz. Detailes modeling of pah profiles in a sooting low-pressure acetylene flame. *Combust. Sci. and Tech.*, 51:265–283, 1987.

[31] N. A. Fuchs. *The Mechanics of Aerosols*. Pergamon Press, 1964.

[32] A. Garo, G. Prado, and J. Lahaye. Chemical aspects of soot particle oxidation in a laminar methane-air flame. *Combustion and Flame*, 79:226–233, 1990.

[33] I. Glassmann. Soot formation in combustion processes. In *Twenty-Second Symposium (International) on Combustion*, pages 295–311. The Combustion Institute, 1988.

[34] I. R. Gran. *Mathematical Modeling and Numerical Simulation of Chemical Kinetics in Turbulent Combustion*. Dr. ing. thesis, University of Trondheim, 1994.

[35] I. R. Gran and B. F. Magnussen. A numerical study of a bluff-body stabilized flame. Part 1. Influence of turbulence modeling and boundary conditions. *Combust. Sci. and Tech.*, 119:171–190, 1996.

[36] I. R. Gran and B. F. Magnussen. A numerical study of a bluff-body stabilized flame. Part 2. Influence of combustion modeling and finite-rate chemistry. *Combust. Sci. and Tech.*, 119:191–217, 1996.

[37] R. J. Hall. Computation of the radiative power of a sooting diffusion flame. *Applied Optics*, 27(5):809–811, 1988.

[38] S. J. Harris. Surface growth and soot particle reactivity. *Combustion Science and Technology*, 72:67–77, 1990.

[39] S. J. Harris and A. M. Weiner. Surface growth of soot particles in premixed ethylene/air flames. *Combust. Sci and Tech*, 31:155–167, 1983.

[40] B. S. Haynes and Wagner H. Gg. Soot formation. *Prog. Energy Combust. Sci.*, 7:229–273, 1981.

[41] B. S. Haynes, H. Jander, and Wagner H. Gg. The effect of metal additives on the formation of soot in premixed flames. In *Seventeenth Symposium (International) on Combustion*, pages 1365–1374, Pittsburgh, 1979. The Combustion Institute.

[42] A. C. Hindmarsh. Odepack, a systematized collection of ode solvers. In R. S Stepleman, editor, *Scientific Computing*, pages 55–64. North Holland, Amsterdam, 1983.

[43] J.O. Hirschfelder, C.F. Curtiss, and R.B. Bird. *Molecular Theory of Gases and Liquids*. John Wiley & Sons, New York, second edition, 1964.

[44] K. H. Homann and H. GG. Wagner. Some new aspects of the mechanism of carbon formation in premixed flames. In *Eleventh Symposium (International) on Combustion*, pages 371–379, Pittsburgh, 1967. The Combustion Institute.

[45] H. C. Hottel and A. F. Sarofim. *Radiative Transfer*. McGraw-Hill Book Company, 1967.

[46] F. P. Incropera and D. P. DeWitt. *Fundamentals of Heat and Mass Transfer*. John Wiley & Sons, third edition, 1990.

[47] W. P. Jones and B. E. Launder. The prediction of laminarization with a two-equation model of turbulence. *International Journal of Heat and Mass Transfer*, 15:301–314, 1972.

[48] I. M. Kahn, G. Greeves, and D. M. Probert. In *Air Pollution Control in Transport Engines*, pages 205–217, London, 1971. The Institution of Mechanical Engineers.

[49] Robert J. Kee, Fran M. Rupley, and James A. Miller. CHEMKIN-II. Sandia Report SAND89-8009, Sandia National Laboratories, Livermore, 1989.

[50] I. M. Kennedy. Models of soot formation and oxidation. *Prog. Energy Combust. Sci.*, 23, 1997.

[51] J. H. Kent and D. Honnery. Soot and mixture fraction in turbulent diffusion flames. *Combust. Sci. and Tech.*, 54:383–397, 1987.

[52] W. Kollmann, I. M. Kennedy, M. Metternich, and J.-Y. Chen. Application of a soot model to a turbulent ethylene diffusion flame. In *Soot Formation in Combustion*, pages 503–526. Springer-Verlag, 1994.

[53] A. Kronenburg, R. W. Bilger, and J. H. Kent. Modeling soot formation in turbulent methane-air jet diffusion flames. *Combustion and Flame*, 121:24–40, 2000.

[54] K. K. Kuo. *Principles of Combustion*. John Wiley & Sons, New York, 1986.

[55] B. E. Launder and D. B. Spalding. The numerical computation of turbulent flows. *Computer Methods in Appl. Mech. and Eng.*, 3:269–289, 1974.

[56] K. M. Leung, R. P. Lindstedt, and W. P. Jones. A simplified reaction mechanism for soot formation in nonpremixed flames. *Combustion and Flame*, 87:289–305, 1991.

[57] S. K. Liew, K. N. C. Bray, and J. B. Moss. A stretched laminar flamelet model of turbulent nonpremixed combustion. *Combustion and Flame*, 56:199–213, 1984.

[58] B. Lilleberg. Matematisk modellering og numerisk simulering av danning og reduksjon av nitrogenoksid i forbrenning. Master's thesis, Norwegian University of Science and Technology, Trondheim, Norway, 2002.

[59] N. I. Lilleheie, J. Holen, and B. F. Magnussen. Multi-species version of Kameleon-FireEx with emphasis on combustion and soot modeling. Technical report, SINTEF Energy, 1997.

[60] R. P. Lindstedt. Simplified soot nucleation and surface growth steps for non-premixed flames. In H. Bockhorn, editor, *Soot Formation in Combustion*, pages 417–441. Springer-Verlag, 1994.

[61] R.P. Lindstedt and G. Skevis. Chemistry of acetylene flames. *Combust. Sci. and Tech.*, 125:73–137, 1997.

[62] B. F. Magnussen. An investigation into the behavior of soot in a turbulent free jet C_2H_2-flame. In *Fifteenth Symposium (International) on Combustion*, pages 1415–1425, Pittsburgh, 1975. The Combustion Institute.

[63] B. F. Magnussen. On the structure of turbulence and a generalized eddy dissipation concept for chemical reaction in turbulent flow. Presented at the *19th American Institute of Aeronautics and Astronautics Aerospace Science Meeting*, St. Louis, Missouri, USA, 1981.

[64] B. F. Magnussen. Modeling of pollutant formation in gas turbine combustors based on the eddy dissipation concept. In *Eighteenth International Congress on Combustion Engines*, Tianjin, China, June 1989. International Council on Combustion Engines.

[65] B. F. Magnussen and B. H. Hjertager. On mathematical modeling of turbulent combustion with special emphasis on soot formation and combustion. In *Sixteenth Symposium (International) on Combustion*, pages 719–729, Pittsburgh, 1977. The Combustion Institute.

[66] B. F. Magnussen, B. H. Hjertager, J. G. Olsen, and D. Bhaduri. Effects of turbulent structure and local concentrations on soot formation and combustion in C_2H_2 diffusion flames. In *Seventeenth Symposium (International) on Combustion*, pages 1383–1393, Pittsburgh, 1979. The Combustion Institute.

[67] F. Mauss, B. Trilken, H. Breitbach, and N. Peters. Soot formation in partially premixed diffusion flames at atmospheric pressure. In *Soot Formation in Combustion*, pages 325–349. Springer-Verlag, 1994.

[68] M. C. Melaaen. *Analysis of Curvilinear Non-orthogonal Coordinates for Numerical Calculation of Fluid Flow in Complex Geometries*. Dr. ing. thesis, University of Trondheim, Norway, 1990.

[69] M. C. Melaaen. Calculation of fluid flows with staggered and nonstaggered curvilinear nonorthogonal grids – a comparison. *Numerical Heat Transfer, Part B*, 21:21–39, 1992.

[70] M. C. Melaaen. Calculation of fluid flows with staggered and nonstaggered curvilinear nonorthogonal grids – the theory. *Numerical Heat Transfer, Part B*, 21:1–19, 1992.

[71] J. A. Miller and Melius C. F. Kinetic and thermodynamic issues in the formation of aromatic compounds in flames of aliphatic fuels. *Combustion and Flame*, 91:21–39, 1992.

[72] A. P. Morse. PhD thesis, London University, 1980.

[73] J. B. Moss, C. D. Stewart, and K. J. Syed. Flowfield modelling of soot formation at elevated pressure. In *Twenty-Second Symposium (International) on Combustion*, pages 413–422. The Combustion Institute, 1988.

[74] M. J. Mran and H. N. Shapiro. *Fundamentals of Engineering Thermodynamics*. John Wiley & Sons Ltd, third edition, 1998.

[75] T. Myhrvold, I. S. Ertesvåg, I. R. Gran, R. Cabra, and J.-Y. Chen. A numerical investigation of a lifted H_2/N_2 turbulent jet flame in a vitiated coflow. submitted to *Combust. Sci. Technol.*

[76] J. Nagle and R. F. Strickland-Constable. Oxidation of carbon between 1000 and 2000 ∘c. In *Proc. 5th Carbon Conf.*, volume 1, pages 154–164, 1962.

[77] S. V. Patankar. *Numerical Heat Transfer and Fluid Flow*. Hemisphere, Washington, 1980.

[78] R. H. Perry and C. H. Chilton. *Chemical Engineers' Handbook*. McGraw-Hill Book Company, fifth edition, 1973.

[79] H. Pitsch, E. Riesmeier, and N. Peters. Unsteady flamelet modeling of soot formation in turbulent diffusion flames. *Combust. Sci. and Tech.*, 158:389–406, 2000.

[80] S. B. Pope. An explanation of the turbulent round-jet/plane-jet anomaly. *AAIJ*, 16(3):279–281, 1978.

[81] L. Prandtl. Über ein neues formelsystem für die ausgebildeten turbulenz. *Nachrichten Akad. Wiss. Göttingen, Matem.-phys.*, pages 6–19, 1945.

[82] R. Puri, R. J. Santoro, and K. C. Smyth. The oxidation of soot and carbon monoxide in hydrocarbon diffusion flames. *Combustion and Flame*, 97:125–244, 1994.

[83] C. M. Rhie and W. L. Chow. Numerical study of the turbulent flow past an airfoil with trailing edge separation. *AIAA Journal*, 21(11), 1983.

[84] O. Roditcheva. *Numerical Modelling of Soot Formation in Turbulent Non-Premixed Flames*. PhD thesis, Lund Institute of Technology, Dept. of Heat and Power Eng., 2000.

[85] O. V. Roditcheva and X. S. Bai. Pressure effect on soot formation in turbulent diffusion flames. *Chemosphere*, 42:811–821, 2001.

[86] J. R. Rostrup-Nielsen, J. Sehested, and J. K. Nørskov. Hydrogen and synthesis gas by steam- and CO_2 reforming. *Adv. Catal.*, pages 65–109, 2002.

[87] Pope. S. *Turbulent Flows*. Cambridge University Press, 2000.

[88] R. Said, A. Garo, and R. Borghi. Soot formation modeling for turbulent flames. *Combustion and Flame*, 108:71–86, 1997.

[89] R. Siegel and J. R. Howell. *Thermal Radiation and Heat Transfer*. McGraw-Hill Book Company, second edition, 1981.

[90] N. Smith, J. Gore, JM. Kim, and Tang. Q. International workshop on measurement and computation of turbulent nonpremixed flames. `http://www.ca.sandia.gov/TNF/radiation.html`. Last visited 15 August 2005.

[91] M. Smoluchowski. Stability and instability in dispersed systems. *Z. Phys. Chem.*, 92:129–136, 1917.

[92] K. J. Syed, C. D. Stewart, and J. B. Moss. Modelling soot formation and thermal radiation in buoyant turbulent diffusion flames. In *Twenty-Third Symposium (International) on Combustion*, pages 1533–1541. The Combustion Institute, 1990.

[93] H. Tennekes and J. L. Lumley. *A First Course in Turbulence*. MIT Press, Cambridge, Massachusetts, and London, England, 1972. Fourteenth printing, 1992.

[94] P. A. Tesner, T. D. Snegiriova, and V. G. Knorre. Kinetics of dispersed carbon formation. *Combustion and Flame*, 17:253–260, 1971.

[95] P. A. Tesner, L. P. Tsygankova, L. P. Guilazetdinov, V. P. Zuyev, and G. V. Loshakova. The formation of soot from aromatic hydrocarbons in diffusion flames of hydrocarbon-hydrogen mixtures. *Combustion and Flame*, 17:279–285, 1971.

[96] B. E. Vembe. *A Generic Preprocessor for Computational Fluid Dynamics*. Dr. ing. thesis, University of Trondheim, Norway, 1993.

[97] J. Warnatz, U. Maas, and R. W. Dibble. *Combustion*. Springer-Verlag, Berlin Heidelberg, third edition, 2001.

[98] B. L. Wersborg, J. B. Howard, and G. C. Williams. Physical mechanisms in carbon formation in flames. In *Fourteenth Symposium (International) on Combustion*, pages 929–940, Pittsburgh, 1973. The Combustion Institute.

[99] F. M. White. *Fluid Mechanics*. McGraw-Hill, Inc., second edition, 1988.

[100] F. Xu, A. M. El-Leathy, C. H. Kim, and G. M. Faeth. Soot surface oxidation in hydrocarbon/air diffusion flames at atmospheric pressure. *Combustion and Flame*, 132:43–57, 2003.

[101] F. Xu, P. B. Sunderland, and G. M. Faeth. Soot formation in laminar premixed ethylene / air flames at atmospheric pressures. *Combustion and Flame*, 108:471–493, 1997.

[102] K. J. Young and J. B. Moss. Modelling sooting turbulent jet flames using an extended flamelet technique. *Combust. Sci. and Tech*, 105:33–53, 1995.